Obliquity forcing of organic matter accumulation during Oceanic Anoxic Event 2

Stephen R. Meyers,[1] Bradley B. Sageman,[2] and Michael A. Arthur[3]

Received 16 January 2012; revised 12 June 2012; accepted 18 June 2012; published 14 August 2012.

[1] An analysis of orbitally influenced climate-sensitive sedimentation is conducted across a meridional transect of the proto-North Atlantic, to reconstruct the behavior of the carbon cycle and climate during Oceanic Anoxic Event 2 (OAE 2; ~94 Ma). Midlatitude to near equatorial sites spanning deep-ocean to shelf environments are evaluated using a new inverse method for the identification and calibration of orbital influence in ancient strata. The results yield consistent independent astrochronologies at each location—compatible with the recently published radioisotopic/astrochronologic time scale at the Cenomanian-Turonian GSSP—and thus provide a unified high-resolution temporal context for evaluation of the event. The proto-North Atlantic astrochronologies document an amplification of obliquity power during OAE 2, indicating that obliquity was the dominant pacemaker of organic matter accumulation by the latter portion of the event. The strong obliquity signal suggests an influence of high-latitude climate processes across midlatitude deep-ocean to tropical shelf environments. Changes in oceanic circulation during OAE 2 represent a likely mechanism for the propagation of a high latitude signal, and proxy data from Demerara Rise reveal the development of a new intermediate water mass source synchronous with the record of obliquity amplification. We hypothesize that a dense high-latitude water mass displaced a pre-existing nutrient-rich anoxic deep-water layer in the proto-North Atlantic (augmented by enhanced volcanism), driving an episode of high productivity that lasted 700–800 ka. The development and intensification of the new intermediate/deep water source was potentially driven by eustatic sea level rise, which created expansive seaways in mid to high latitudes.

Citation: Meyers, S. R., B. B. Sageman, and M. A. Arthur (2012), Obliquity forcing of organic matter accumulation during Oceanic Anoxic Event 2, *Paleoceanography*, *27*, PA3212, doi:10.1029/2012PA002286.

1. Introduction

[2] OAE 2 represents an extreme perturbation to the global carbon cycle, characterized by widespread deposition of organic carbon-rich marine sediments, and a pronounced positive carbon isotope excursion [*Arthur et al.*, 1987]. Due to the common occurrence of rhythmic marine sedimentation within the OAE 2 interval, this event has emerged as a model case study for the investigation of paleoceanographic events via the integration of high-resolution orbital time scales with paleobiologic and geochemical data [e.g., *Meyers et al.*, 2001; *Tsikos et al.*, 2004; *Meyers et al.*, 2005; *Kolonic et al.*, 2005]. One of the key challenges hindering development of an accurate global synthesis of this event is the inconsistency of orbital chronologies developed for different localities [*Kauffman*, 1995; *Gale*, 1995; *Kuhnt et al.*, 1997; *Meyers et al.*, 2001; *Prokoph et al.*, 2001; *Tsikos et al.*, 2004; *Kuypers et al.*, 2004; *Sageman et al.*, 2006; *Nederbragt et al.*, 2007; *Voigt et al.*, 2008]. In order to correlate OAE 2 records across large spans of paleolatitude, and at a resolution sufficient to address leads and lags in the climate system, a consistent and objective methodology for calibration of observed spatial rhythms to temporal periods is needed. In the present study, we introduce a new time-frequency implementation of the "Average Spectral Misfit" method (or ASM) [*Meyers and Sageman*, 2007], which allows us to quantitatively test for the presence of orbital influence on sedimentation during OAE 2. The method does not require rigorous supplementary time control, provides a means to objectively and independently calibrate the orbital chronometers at widely separated sites, and is specifically designed to evaluate orbital signals that are distorted by unsteady sedimentation rate histories.

[3] We have selected three primary stratigraphic data sets for this analysis (Figures 1 and 2), based on the superior quality of the records and their geographic distribution:

[1]Department of Geoscience, University of Wisconsin-Madison, Madison, Wisconsin, USA.
[2]Department of Earth and Planetary Sciences, Northwestern University, Evanston, Illinois, USA.
[3]Department of Geosciences, Pennsylvania State University, University Park, Pennsylvania, USA.

Corresponding author: S. R. Meyers, Department of Geoscience, University of Wisconsin-Madison, 1215 W. Dayton St., Madison, WI 53706, USA. (smeyers@geology.wisc.edu)

0883-8305/12/2012PA002286

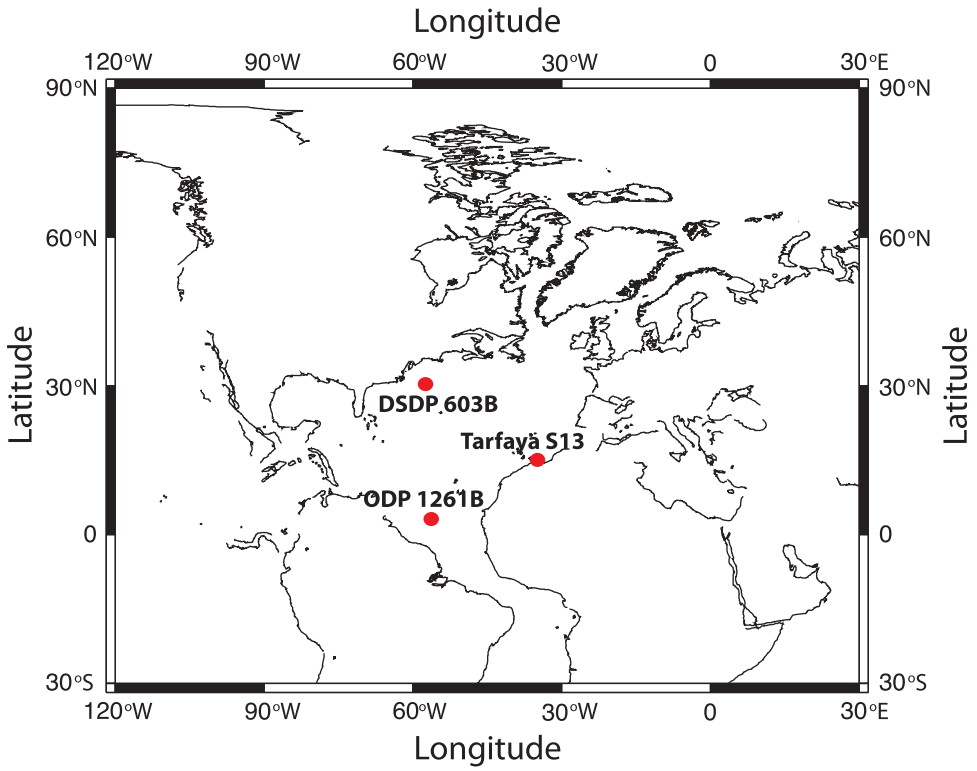

Figure 1. Paleogeographic map (94 Ma) with the locations of the three sites investigated in this study: DSDP site 603B, Tarfaya S13 from Morocco, and ODP 1261B from Demerara Rise. The map was constructed using the GEOMAR map generator (www.odsn.de/odsn/services/paleomap/paleomap.html).

(1) published weight percent total organic carbon data [*Herbin et al.*, 1987] from the midlatitude proto-North Atlantic (DSDP site 603B at ~30°N paleolatitude; Figure 2a), (2) a density well log from Morocco (Tarfaya S13 core, Figure 2b), which primarily reflects changes in organic carbon versus carbonate content of strata in a near-equatorial (~15°N paleolatitude) eastern proto-North Atlantic coastal upwelling setting [*Kuhnt et al.*, 1997], and (3) a Formation MicroScanner well log from Demerara Rise (ODP site 1261B; Figure 2c), which records oscillations between organic carbon-rich shale and organic carbon-poor limestone in a near-equatorial (~5°N paleolatitude) western proto-North Atlantic coastal upwelling setting [*Shipboard Scientific Party*, 2004]. Taken together these records provide a hemispheric transect that spans mid to low latitude sites, and of note, all high-resolution data sets investigated here directly or indirectly provide a measure of the organic-carbon richness of the strata.

[4] As will be demonstrated below, application of the new methodology results in a critical advancement toward the global synthesis of previously disparate Cenomanian/Turonian (C/T) astrochronologies, and provides a new opportunity to evaluate mechanisms of paleoceanographic change associated with OAE 2. In particular, assessment of the resultant astrochronologies reveals an amplification of obliquity forcing during OAE 2 at all sites, suggesting the influence of high-latitude climate processes on sedimentation across midlatitude deep ocean to tropical shelf environments. Potential mechanisms for generating the strong obliquity response include enhanced high-latitude intermediate/deep-water formation and/or polar ice sheet growth associated with the carbon burial event, topics that will be further considered herein.

[5] The organization of the paper is as follows: Section 2 briefly summarizes the Average Spectral Misfit Method of *Meyers and Sageman* [2007], with a number of important improvements and a special emphasis on the treatment of stratigraphic sections characterized by unsteady sedimentation rate histories. Section 3 presents details of the astrochronologic analysis of the three sites that are investigated herein (DSDP 603B, Tarfaya, Demerara Rise). Section 4 provides a more condensed summary and comparison of the astrochronologic calibrations at each site. Section 5 presents an assessment of the influence of obliquity forcing at each location, and the integration of our new results with existing paleoceanographic data to explore mechanisms for the observed obliquity amplification.

2. Methodology: Evolutive Average Spectral Misfit

[6] A wide range of factors can complicate assessment of orbital-insolation influence on sedimentation [*Herbert*, 1994; *Muller and MacDonald*, 2000; *Meyers et al.*, 2001; *Weedon*, 2003; *Meyers and Sageman*, 2004, 2007; *Meyers et al.*, 2008]. The absence of adequate independent chronostratigraphic control (e.g., radioisotopic data with sufficiently small errors, highly resolved biostratigraphy) to calibrate observed spatial rhythms to temporal periods is one of the most daunting challenges to a quantitative test of the orbital hypothesis. In lieu of such information, a common approach

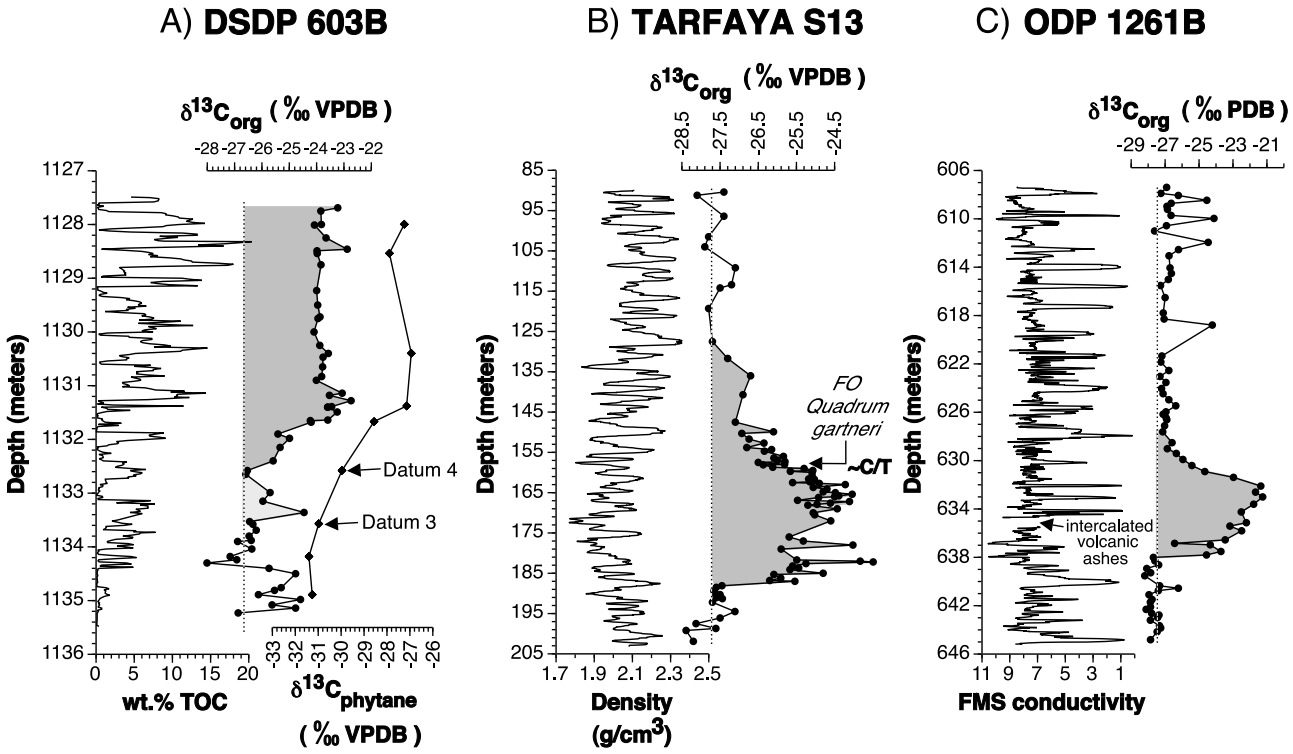

Figure 2. (a) Weight percent total organic carbon (wt.% TOC) [*Herbin et al.*, 1987], the carbon isotopic value of bulk organic matter (new isotopic data combined with data previously published by *Kuypers et al.* [2004]) ($\delta^{13}C_{org}$; per mil VPDB), and the carbon isotopic value of sulfur-bound phytane ($\delta^{13}C_{phytane}$; per mil VPDB) for samples from the upper portion of the Hatteras Formation at DSDP Site 603B [*Kuypers et al.*, 2004]. "Datum 3" and "Datum 4" constrain the initiation of OAE 2 as defined by $\delta^{13}C_{phytane}$. (b) New density data (g/cm^3) (kindly provided by Prof. Wolfgang Kuhnt) and the carbon isotopic value of bulk organic matter ($\delta^{13}C_{org}$; per mil VPDB) for Cenomanian/Turonian strata in the Tarfaya S13 core [*Kolonic et al.*, 2005]. The location of the C/T boundary is based on the first occurrence of the nannofossil *Quadrum gartneri* [*Kolonic et al.*, 2005]. (c) FMS data (uncalibrated conductivity) [*Shipboard Scientific Party*, 2004] and the carbon isotopic value of bulk organic matter ($\delta^{13}C_{org}$; per mil PDB) [*Erbacher et al.*, 2005] for Cenomanian/Turonian strata at Demerara Rise ODP Site 1261B.

is to evaluate power spectra of lithologic, paleobiologic, or geochemical data series, especially the frequency ratios of dominant peaks. The agreement of observed ratios with proposed orbital frequency ratios, such as the 5:1 relationship for short eccentricity (~100 ka) and precession (~20 ka), is commonly taken as confirmation of orbital influence. While this seemingly straightforward approach may be successful under some circumstances, the appropriate orbital interpretation of power spectra is not always obvious. As a consequence, multiple incompatible orbital interpretations exist for some stratigraphic units (e.g., *Meyers et al.* [2001] versus *Prokoph et al.* [2001]; *Preto et al.* [2001] versus *Zühlke et al.* [2003] versus *Kent et al.* [2004]). Furthermore, such simplistic "frequency ratio" methods do not explicitly consider the degree of alignment required for a "good fit," nor do they provide any estimate of the significance of the fit [see *Meyers and Sageman*, 2007].

[7] Average spectral misfit (ASM) [*Meyers and Sageman*, 2007] is an inverse method designed to quantify the alignment between a target orbital spectrum and the measured spectral peaks observed in a stratigraphic series, given a range of plausible sedimentation rates. The metric is measured in cycles/ka, and represents the average distance (or "misfit") between the target and measured spectrum peaks, while explicitly accounting for the resolution limitations inherent in the spectral analysis. Our implementation of the ASM method is adapted from *Meyers and Sageman* [2007], and is defined as

$$ASM = \frac{1}{N}\sum_{k=1}^{N}\alpha_k \tag{1}$$

$$\alpha_k = \begin{cases} 0 & \text{if } \left|(f^*s - f_{pred}\right| \le 0.5^*\Delta f_R^*s \\ \min\left\{\left|(f^*s + 0.5^*\Delta f_R^*s) - f_{pred}\right|, \left|(f^*s - 0.5^*\Delta f_R^*s) - f_{pred}\right|\right\} & \text{if } \left|(f^*s - f_{pred}\right| > 0.5^*\Delta f_R^*s \end{cases} \tag{2}$$

where

N = number of orbital periods evaluated in the ASM analysis;

f = spatial frequency peak location (cycles/m);

s = sedimentation rate (m/ka);

f_{pred} = predicted orbital frequency (cycles/ka);

Δf_R = spatial frequency resolution bandwidth (cycles/m);

α_k = distance (in cycles/ka) between the location of the predicted orbital component and the closest significant peak in the spectrum.

[8] Significance levels for rejection of the null hypothesis (no orbital signal) are estimated with Monte Carlo spectra simulations. The simulated spectra have the same resolution limitations (Nyquist frequency and Rayleigh resolution) as the measured spectrum, but contain spectral peaks distributed at random frequencies. ASM probability distributions for each temporal calibration are constructed using the simulated spectra, and the null hypothesis (H_O) significance levels indicate how frequently a particular ASM value should occur by chance, given a spectrum with peaks distributed at random frequencies (see *Meyers and Sageman* [2007] for further details).

[9] The ASM methodology outlined above is philosophically similar to a Bayesian approach introduced by *Malinverno et al.* [2010]. Whereas the ASM method seeks to identify the sedimentation rate that minimizes the misfit between the observed frequencies and predicted orbital components, the *Malinverno et al.* [2010] technique instead seeks to maximize the likelihood of the sedimentation rate model. The two approaches are complimentary: whereas the Bayesian likelihood analysis includes a measure of the uncertainty of the inferred sedimentation rate, the ASM method provides a rigorous significance test for the presence of astronomical cycles.

[10] In this study we introduce four important improvements to the ASM methodology originally proposed in *Meyers and Sageman* [2007]. First, to enhance the sensitivity of the method, equation 2 includes a new parameterization of α_k that better incorporates the uncertainty in the measured spectrum peak locations. Second, a log-scaling of sedimentation rate is implemented for the ASM grid search optimization to better evaluate rapid ASM variability that is commonly observed at low sedimentation rates [e.g., see *Meyers*, 2008]. The cause of this rapid ASM variability at low sedimentation rates is twofold. Foremost, as sedimentation rate decreases the effective length of the time series increases, resulting in a smaller temporal frequency resolution bandwidth (cycles/ka); this reduction in the resolution bandwidth naturally increases the sensitivity of the spectrum. In addition, the temporal Nyquist frequency (cycles/ka) decreases with sedimentation rate, which can result in a rapid loss of orbital terms available for ASM calculation at low sedimentation rates. The effect of these phenomena can be especially pronounced when investigating broad ranges of sedimentation rate, and it is therefore advantageous to conduct a more detailed ASM grid search at lower sedimentation rates, while a coarser ASM grid search at higher sedimentation rates is sufficient.

[11] The ASM method indicates the most plausible average sedimentation rate for a stratigraphic interval, given a particular orbital model. Although the technique can accommodate substantial fluctuations in sedimentation rate (e.g., 33%) [*Meyers and Sageman*, 2007], when the orbital signal is severely distorted by sedimentation rate changes, the method will ultimately fail to reject the null hypothesis with a high degree of confidence. In the present study, we develop an approach to evaluate orbital signals that are distorted by unstable sedimentation histories. To do so, ASM analysis is performed on a data window that is shifted sequentially through the study interval. This approach is designated "Evolutive ASM," and provides a comprehensive test of the null hypothesis (no orbital signal) across the entire time-frequency parameter space. Thus, Evolutive ASM explicitly accommodates for changes in sedimentation rate throughout the study interval, and provides the ability to prospect for portions of the stratigraphic record with high signal/noise [i.e., *Meyers et al.*, 2008]. When astronomical cycles can be quantitatively confirmed in a portion of the stratigraphic record using this approach, it is also possible to extend those calibrated signals into other portions of the stratigraphy, if time frequency analysis (e.g., Evolutive Harmonic Analysis) [*Meyers et al.*, 2001] indicates that the bedding cycles are persistent.

[12] The fourth improvement to the ASM technique pertains to the theoretical orbital target frequencies (f_{pred}) and their uncertainties. In the present study we evaluate and compare two theoretical astronomical models for the late Cretaceous, the frequency domain model of *Berger et al.* [1992], and time domain model of *Laskar et al.* [2004, 2011]. Importantly, the astronomical model of *Laskar et al.* [2004, 2011] permits a quantification of frequency uncertainty [e.g., *Malinverno et al.*, 2010] that can be incorporated in the ASM analysis. Following the approach of *Malinverno et al.* [2010], we estimate mean values and 2σ uncertainties for seven late Cretaceous astronomical periods observed in the *Laskar et al.* [2004, 2011] solutions (Table S1 in the auxiliary material).[1] The two dominant precession frequencies and two dominant obliquity frequencies are evaluated via multitaper method (MTM) [*Thomson*, 1982] harmonic analysis of four 0.5 Ma segments of the *Laskar et al.* [2004] solution (93–93.5 Ma, 93.5 Ma–94 Ma, 94 Ma–94.5 Ma, 94.5–95 Ma). *Laskar et al.* [2011] provide four new candidate eccentricity solutions, each of which is evaluated in 1 Ma segments (93–94 Ma, 94–95 Ma) to yield eight estimates of the two dominant short eccentricity terms, and 2 Ma segments (93–95 Ma) are used to provide four estimates of the long eccentricity frequency (longer analysis intervals are required for the eccentricity terms to provide suitable estimates of their periods). Finally, we compare these results to the late Cretaceous (94 Ma) precession and obliquity periods proposed by *Berger et al.* [1992]. Table S1 in the auxiliary material provides a summary of the theoretical astronomical target frequencies used in our cyclostratigraphic study of OAE 2.

[13] Finally, a key step in conducting an ASM analysis is the selection of significant spatial bedding frequencies (cycles/m) for cyclostratigraphic evaluation. In this study we use the MTM harmonic test of *Thomson* [1982] for this purpose, and consistent with previous work [*Meyers and*

[1]Auxiliary materials are available in the HTML. doi:10.1029/2012PA002286.

Sageman, 2007; *Meyers*, 2008] we use a confidence level (also referred to as probability) of 90% to identify significant bedding frequencies, unless otherwise noted. Relevant to this issue, a number of studies highlight the fact that the conventional spectrum confidence levels used in paleoclimatology/cyclostratigraphy [e.g., *Hays et al.*, 1976; *Park and Herbert*, 1987; *Thomson*, 1990; *Hinnov and Goldhammer*, 1991; *Sageman et al.*, 1997; *Weedon and Jenkyns*, 1999] are susceptible to high false positive rates [*Thomson*, 1990, 2010; *Muller and MacDonald*, 2000; *Mudelsee*, 2010; *Vaughan et al.*, 2011]. A more detailed consideration of this important issue is provided in *Meyers* [2012], but here we note that the ASM approach recognizes an important distinction between testing the astronomical hypothesis, and prospecting for unknown 'cycles' – those that are not predicted based on a physical model. In the case of the former, there are additional features of the astronomical signal (beyond peak significance) that can be utilized in hypothesis testing [*Hinnov*, 2000]. Following the ASM approach, observed spatial bedding periods are considered *candidate* astronomical cycles, which may or may not represent orbital influence, regardless of the peak significance. Importantly, the ASM Monte Carlo simulations provide an explicit evaluation of the astronomical hypothesis.

3. Astrochronologic Evaluation of the Proto-North Atlantic

3.1. DSDP 603B: The Midlatitude Deep Ocean Signal of the Proto-North Atlantic

[14] DSDP site 603B is located on the lower continental rise (4642 m water depth), 270 nautical miles east of Cape Hatteras in the Atlantic Ocean. Coring at this site during Leg 93 recovered alternating green and black shales of the Hatteras Formation, including strata of late Cenomanian (and possibly early Turonian) age [*Herbin et al.*, 1987]. Carbon isotopic analysis of bulk organic matter (*Kuypers et al.* [2004] plus new data from this study) and sulfur-bound phytane at 603B [*Kuypers et al.*, 2004] indicate that the site captures the initiation of the OAE 2 isotopic excursion, and much of the main plateau of the excursion, although the end is absent due to a coring gap (Figure 2a). The C/T boundary has not been located at this site, and the precise stratigraphic level of the excursion initiation is questionable, but here we constrain the initiation to be between "Datum 3" and "Datum 4" as demarcated in Figure 2.

[15] High-resolution (2 cm sampling interval) wt.% $CaCO_3$, wt.% organic carbon (OC) and hydrogen index (HI) data have been generated for the upper portion of the Hatteras Formation at site 603B [*Herbin et al.*, 1987]. Of these records, the wt.% OC and HI data have been previously analyzed for bedding cyclicity by *Kuypers et al.* [2004], resulting in identification of three prominent bedding cycles between 0 and 3 cycles/m: ~280 cm, ~75 cm and ~40 cm. The authors interpreted the 75 cm cycle to reflect obliquity forcing (~39 ka) and proposed a sedimentation rate of 1.9 cm/ka.

[16] We select the wt.% OC data for time series analysis because the accuracy of some of the hydrogen index results has been questioned [*Herbin et al.*, 1987]. An MTM power spectrum for the entire wt.% OC data series, from 0 cycles/meter to the Nyquist frequency of 25 cycles/m, indicates that essentially all of the power is concentrated at frequencies ≤10 cycles/m (Figures 3b and 4b). Evolutive Harmonic Analysis (EHA) [*Meyers et al.*, 2001] identifies several persistent high-probability spatial bedding components, indicating a remarkable stability of sedimentation thorough the study interval (Figures 3d and 3e). The primary source of nonstationarity in this record is due to change in the relative strength of individual components (amplitude) rather than spatial frequency drifting associated with sedimentation rate changes.

[17] Given the stability of sedimentation that characterizes DSDP 603B, ASM analysis is performed on the entire wt.% OC data series (Figures 4c and 4d) across 200 individual sedimentation rates spanning 0.5 to 5 cm/ka. Using the Laskar04/Laskar11 astronomical model, the only ASM value to surpass the critical significance level of 0.5% occurs at a sedimentation rate of 0.80 cm/ka ($H_o = 0.119\%$), associated with a global minimum value of 1.09×10^{-4} cycles/ka (Table S2 in the auxiliary material). Evaluation with the Berger92 model yields similar results, identifying a sedimentation rate of 0.79 cm/ka (Figure S1 and Table S3 in the auxiliary material). Calibration of the spectrum using a sedimentation rate of 0.80 cm/ka (Figure 4e) illustrates all of the expected eccentricity, obliquity and precession components (see also Table S2). The disparity between this new astronomical calibration and that of *Kuypers et al.* [2004] is a consequence of their interpretation of the strong ~40 cm cycle as due to precession (ASM indicates that this is obliquity), the ~75 cm cycle as obliquity (ASM indicates that this is short eccentricity), and the ~280 cm cycle as short eccentricity (ASM indicates that this is long eccentricity).

3.2. Tarfaya S13: The Eastern Proto-North Atlantic Tropical Shelf Signal

[18] The Tarfaya S13 core is from the Tarfaya Atlantic Coastal Basin in Morocco, representing the depocenter of a deep shelf environment (~200–300 m water depth) [*Kuhnt et al.*, 1997; *Einsele and Wiedmann*, 1982; *Kuhnt et al.*, 1990]. As indicated by biostratigraphy and carbon isotopic analysis of organic matter (Figure 2b), this core preserves a relatively complete and expanded section of the C/T boundary interval [*Kuhnt et al.*, 1997, 2005; *Kolonic et al.*, 2005]. The C/T strata at the site are primarily composed of pelagic carbonates with varying amounts of organic carbon (0–20 wt. %) [*Kuhnt et al.*, 1997].

[19] A density log from Tarfaya S13 (20 cm sampling resolution) was previously analyzed by *Kuhnt et al.* [1997] to characterize bedding cyclicity; rock density primarily reflects changes in organic matter versus carbonate content, with lower density values characteristic of more organic matter-rich beds. *Kuhnt et al.* [1997] identified six prominent frequencies in the density log data, and proposed that obliquity (39 ka) was the dominant orbital component in the spectrum, expressed as bedding wavelengths between 4.6 and 5 m. This orbital interpretation yields a sedimentation rate of 11.8 to 12.8 cm/ka for the Tarfaya S13 strata.

[20] In this study, we analyze a new high-resolution density log data series from Tarfaya S13 (~5 cm sampling resolution; kindly generated and provided by Prof. Wolfgang Kuhnt). An MTM power spectrum for the entire data series, from 0 cycles/m to the Nyquist frequency of 10 cycles/m, indicates that essentially all of the power is concentrated at frequencies ≤1 cycles/m (Figure 5b). EHA of the density log

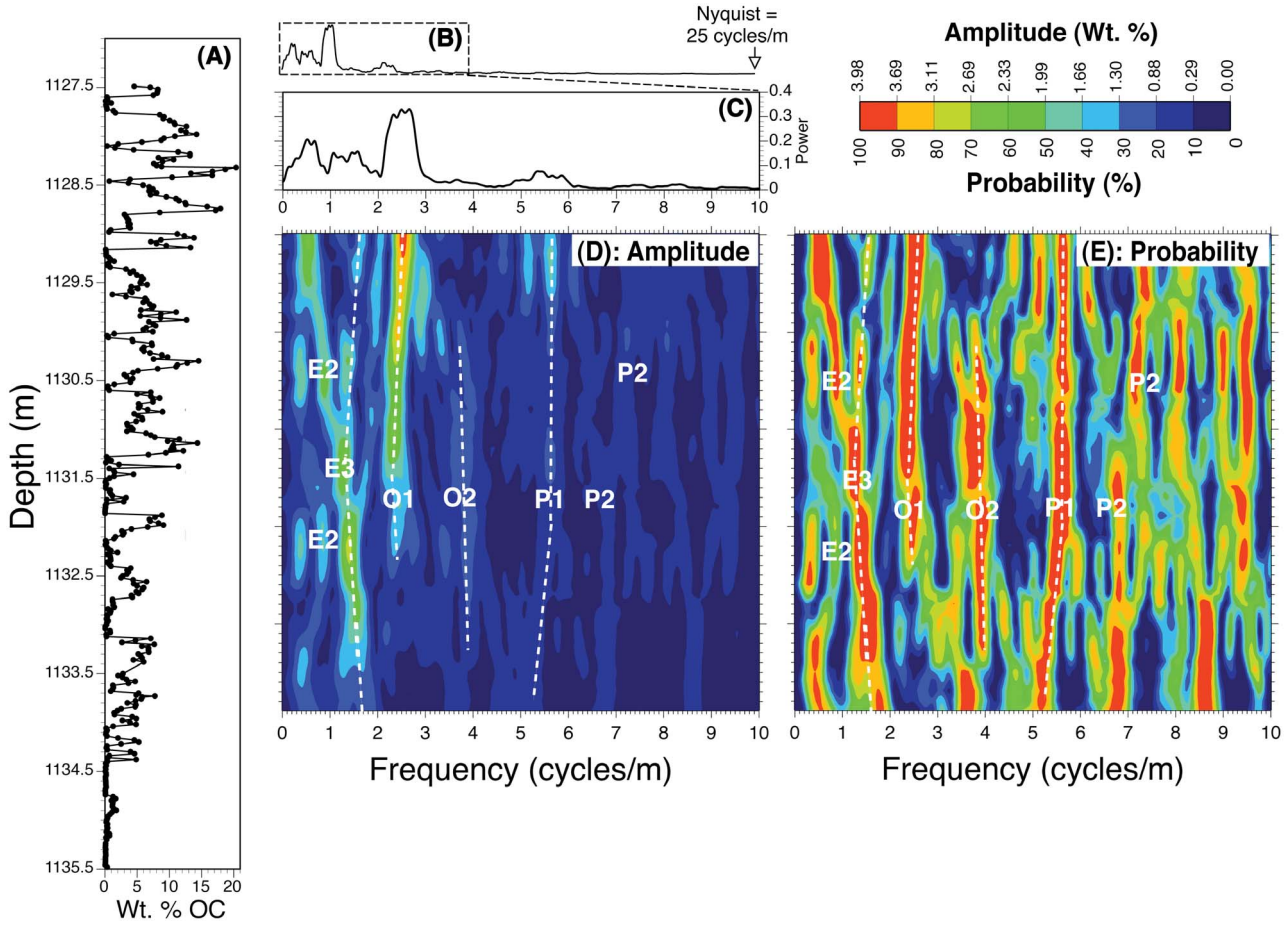

Figure 3. Time series analyses for DSDP Site 603B, in the proto-North Atlantic. (a) The DSDP Site 603B wt.% OC data of *Herbin et al.* [1987]. (b) Five 3π taper MTM power spectrum of the entire wt.% OC data series, plotted from 0 cycles/meter to the Nyquist frequency of 25 cycles/m. (c) Expanded view of this MTM power spectrum from 0 cycles/m to 10 cycles/m. (d) EHA amplitude results using five 3π tapers and a 3-m moving window. (e) EHA probability results using five 3π tapers and a 3-m moving window.

data indicates several persistent and highly significant frequencies, although these bedding periods display some instability (Figures 5d and 5e). In particular, there is a marked shift in the spatial frequencies above 157 m depth, approximately coinciding with the C/T boundary. We hypothesize that this shift is due to an increase in sedimentation rate above 157 m.

[21] Given that the EHA results suggest a pronounced change in sedimentation through the study interval, we utilize the Evolutive ASM approach to evaluate potential astronomical signals. ASM is calculated for the EHA probability results in Figure 5e (177 twenty-five meter windows) across 200 individual sedimentation rates spanning 5 to 25 cm/ka. Using the Laskar04/Lasakar11 orbital target, the procedure identifies an optimal sedimentation rate of 6.07 cm/ka at 179 m depth (H_o significance level = 0.036%), and 9.47 cm/ka at 125 m depth (H_o significance level = 0.060%, Figure 6; see also Figure S2 and Tables S4 and S5 in the auxiliary material). Additional low H_o significance levels are observed at a sedimentation rate of ~15 cm/ka (e.g., ~172 m depth in Figure S2), which is the consequence of localized distortion of the proposed precession terms, and their consequent diminishment below the 90% MTM harmonic probability threshold (Figure 5e). This conclusion is validated by two sensitivity analyses, the first of which excludes the precession terms from the astronomical model, and the second of which includes the precession terms but reduces the MTM harmonic probability threshold to 80% to capture the proposed precession-scale variability (Figure S3). Both analyses unambiguously identify an optimal sedimentation rate of ~6 cm/ka in the lower portion of the Tarfaya record.

[22] Evaluation with the Berger92 model yields similar results, with an optimal sedimentation rate of 5.97 cm/ka at 179 m depth (H_o significance level = 0.011%), and 8.67 cm/ka at 111 m depth (H_o significance level = 0.037%; Figure S2 and Tables S6 and S7). Thus, it is clear that nonstationarity in this record is both a consequence of change in sedimentation rate and change in the relative amplitude of the individual components. Finally, calibration of the spectra using the ASM derived sedimentation rates (Figures 6e and 6j) illustrates all of the expected eccentricity, obliquity and precession components (see also Tables S4 and S5). The disparity between this new astronomical calibration and that of *Kuhnt et al.* [1997] is primarily due to the dramatic sedimentation rate changes that have been identified by Evolutive ASM in the present study.

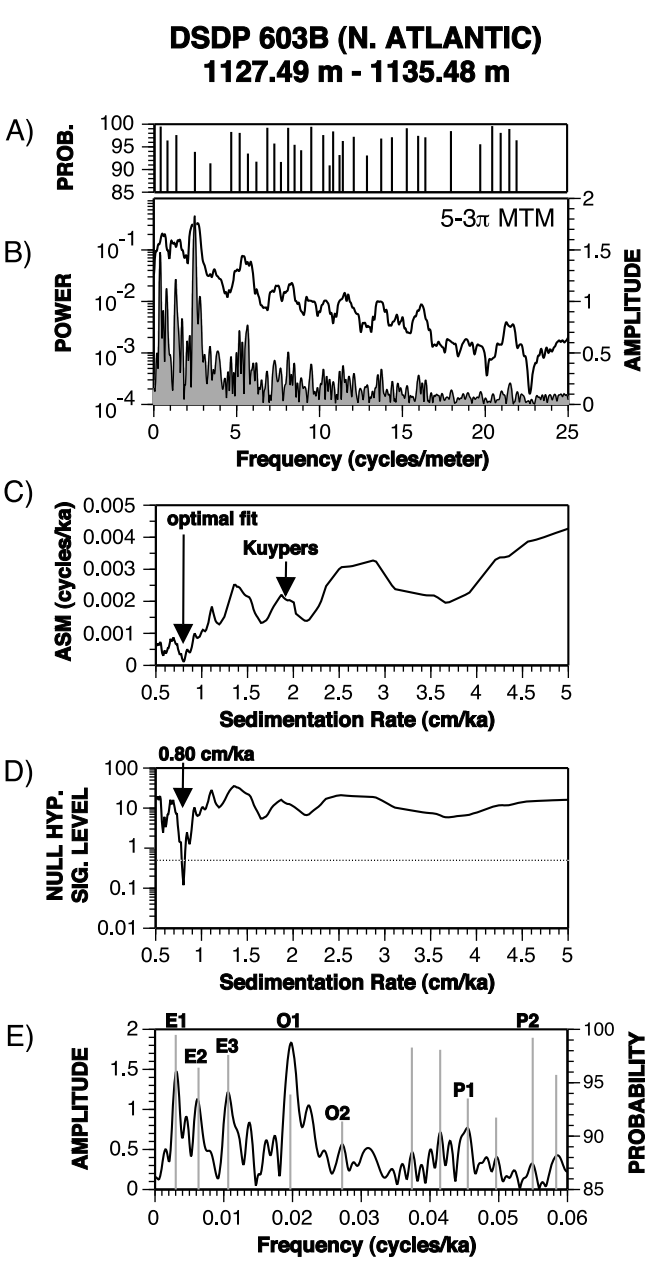

Figure 4. Multitaper method (MTM) spectral analysis and average spectral misfit (ASM) results for the DSDP 603B weight percent OC data series. MTM spectral analysis was conducted using five 3π tapers. ASM evaluates the astronomical model of *Laskar et al.* [2004, 2011], and is calculated for 200 individual sedimentation rates spanning 0.5 to 5 cm/ka, with a log-scaling of the sedimentation rate grid. The null hypothesis Monte Carlo test utilizes 100,000 simulated spectra. (a) MTM harmonic analysis probability results. (b) Log MTM power spectrum estimate (bold line) and amplitude spectrum (gray). (c) Average spectral misfit in cycles/ka "Kuypers" indicates the sedimentation rate proposed by *Kuypers et al.* [2004]. (d) Null hypothesis significance levels. The dotted line indicates a critical significance level of 0.5%. (e) Calibrated amplitude spectrum (black line) and harmonic analysis probability results (vertical lines), using a sedimentation rate of 0.80 cm/ka.

3.3. Demerara Rise ODP Site 1261B: The Western Proto-North Atlantic Tropical Shelf Signal

[23] Site 1261B (ODP Leg 207) is located in the western tropical Atlantic offshore of Suriname. The C/T boundary interval at this site is characterized by interbedded organic carbon-rich finely laminated claystones, organic carbon-poor laminated clayey limestones, and organic carbon-poor clayey chalk, which accumulated in a deep shelf environment [*Shipboard Scientific Party*, 2004]. $\delta^{13}C_{org}$ analysis of Leg 207 core material indicates that Site 1261 preserves the most expanded and complete section of the C/T boundary interval at Demerara Rise (Figure 2c) [*Erbacher et al.*, 2005].

[24] In this study, we analyze a high-resolution Formation MicroScanner (FMS) data series from 1261B (1.27 cm sampling resolution) [*Shipboard Scientific Party*, 2004]. This data series represents the average of 64 electrodes that comprise the FMS sonde, documenting variable conductivity (uncalibrated) through the C/T boundary interval. In general, carbonate-rich beds are characterized by low FMS conductivity values (higher resistivity), while more clay-rich beds are characterized by higher FMS conductivity (lower resistivity) values [e.g., *Locklair and Sageman*, 2008; *Malinverno et al.*, 2010]. The FMS log has been depth shifted by 12.1 m, to account for a previously documented offset between logging and core depths [*Shipboard Scientific Party*, 2004]. Prior to analysis, an interval of volcanic ashes intercalated with chalk (634.7–635.5 mbsf) has been removed and replaced with an average background FMS value for the interval (Figure 2c).

[25] An MTM power spectrum for the entire FMS data series, from 0 cycles/m to the Nyquist frequency of ~39.37 cycles/m, indicates that essentially all of the power is concentrated at frequencies ≤5 cycles/m (Figure 7b). EHA of the 1261B FMS data identifies two distinct stratigraphic intervals: an upper portion from 631 to 610 mbsf that displays several persistent and highly significant frequency components that gradually "drift" to higher frequencies (Figures 7d and 7e), and a lower portion below a depth of 631 mbsf that is characterized by a marked stepwise shift in bedding frequencies. These results suggest a dramatic change in sedimentation between the lower and upper intervals, and a more gradual decrease in sedimentation rate during deposition of the upper interval.

[26] Evolutive ASM is calculated for the EHA probability results in Figure 7e (157 ~6 m windows), across 200 individual sedimentation rates spanning 0.5 to 5 cm/ka. Using the Laskar04/Lasakar11 astronomical target, the procedure identifies an optimal sedimentation rate of 1.48 cm/ka at 612.81 mbsf (H_o significance level = 0.021%), and an optimal sedimentation rate of 1.14 cm/ka at 635.36 mbsf (H_o significance level = 0.077%) (Figure 8; see also Figure S4 and Tables S8 and S9 in the auxiliary material). Evaluation with the Berger92 astronomical model yields similar results (Figure S4 and Tables S10 and S11).

[27] For the strata above 631 mbsf, both astronomical models indicate a number of additional sedimentation rates with H_o significance levels that are only slightly larger than that associated with the 1.48 cm/ka calibration (Figure S4). This is a consequence of the lower signal:noise ratio of the record (as compared to ODP 603B and Tarfaya) and is especially problematic for the higher frequency precession terms

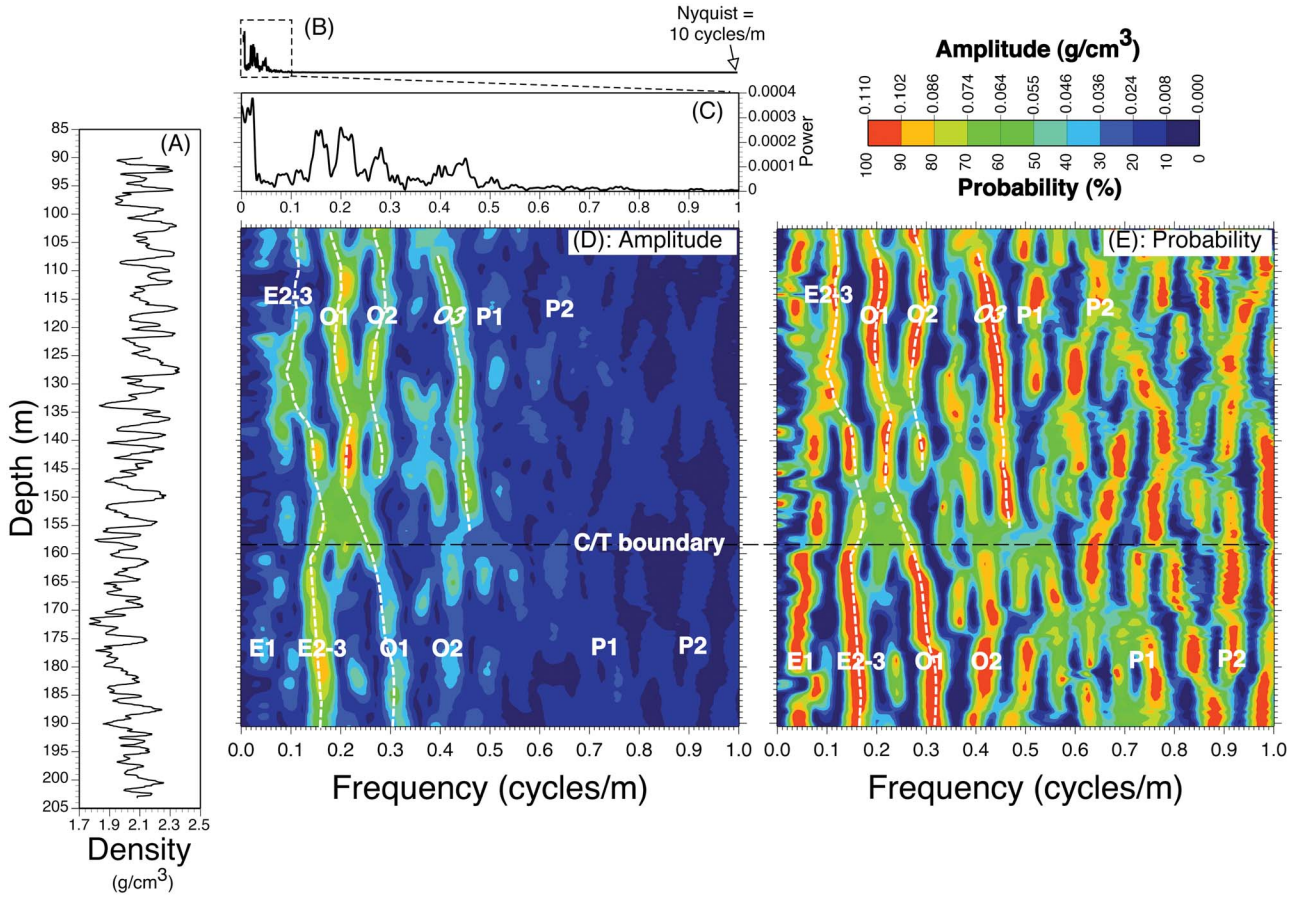

Figure 5. Time series analyses for Tarfaya S13 in Morocco. (a) The density log data for Tarfaya S13. (b) Three 2π taper MTM power spectrum of the entire density log data, plotted from 0 cycles/m to the Nyquist frequency of 10 cycles/m. (c) Expanded view of the MTM power spectrum from 0 to 1 cycle/m. (d) EHA amplitude results using three 2π tapers and a 25-m moving window. (e) EHA probability results using three 2π tapers and a 25-m moving window. Dashed horizontal line identifies the approximate location of the C/T boundary, based on the first occurrence of the nannofossil *Quadrum gartneri* [*Kolonic et al.*, 2005].

that are most sensitive to sedimentation instability. As with the Tarfaya record, we conduct two sensitivity analyses to further constrain the appropriate sedimentation rates, the first of which excludes the precession terms from the astronomical model, and the second of which includes the precession terms in the model but reduces the MTM harmonic probability threshold to 80% to capture the proposed precession-scale variability (Figure S5). These analyses unambiguously identify an optimal sedimentation rate of ~1.43–1.48 cm/ka in the upper portion of the Demerara Rise record.

[28] Calibration of the spectra using the ASM derived sedimentation rates illustrates all of the expected eccentricity, obliquity and precession components (Figures 8e and 8j; see also Tables S8 and S9). This astronomical interpretation is also supported by the observed frequency modulation ("braiding") that is present in the proposed short eccentricity terms (Figure 7d), which is an important feature of the theoretical short eccentricity signal [*Laskar et al.*, 2011] and suggests a relatively pristine record of this astronomical signal. These results differ from previous astrochronologies developed at Demerara Rise [*Nederbragt et al.*, 2007], in part due to the dramatic sedimentation rate changes that have been identified by Evolutive ASM in the present study. It should also be noted that the previous work [*Nederbragt et al.*, 2007] was conducted at sites where the OAE 2 interval is either much thinner or the site did not capture the entire OAE 2 (Sites 1258, 1259 and 1260), and hiatus is also suggested for some intervals [*Erbacher et al.*, 2005; *Nederbragt et al.*, 2007]. We conclude that nonstationarity in the FMS record from Site 1261B is both a consequence of change in sedimentation rate and change in the relative amplitude of the individual components.

4. Summary of the Proto-North Atlantic Astrochronologies

[29] Our analysis of DSDP site 603B reveals relatively stable bedding frequencies throughout the portion of OAE 2 represented in the core (Figure 3), and ASM analysis indicates that it is characterized by the lowest sedimentation rate of the three sites (0.80 cm/ka, H_o = 0.119%; Figure 4), consistent with its deep ocean setting. This sedimentation rate is less

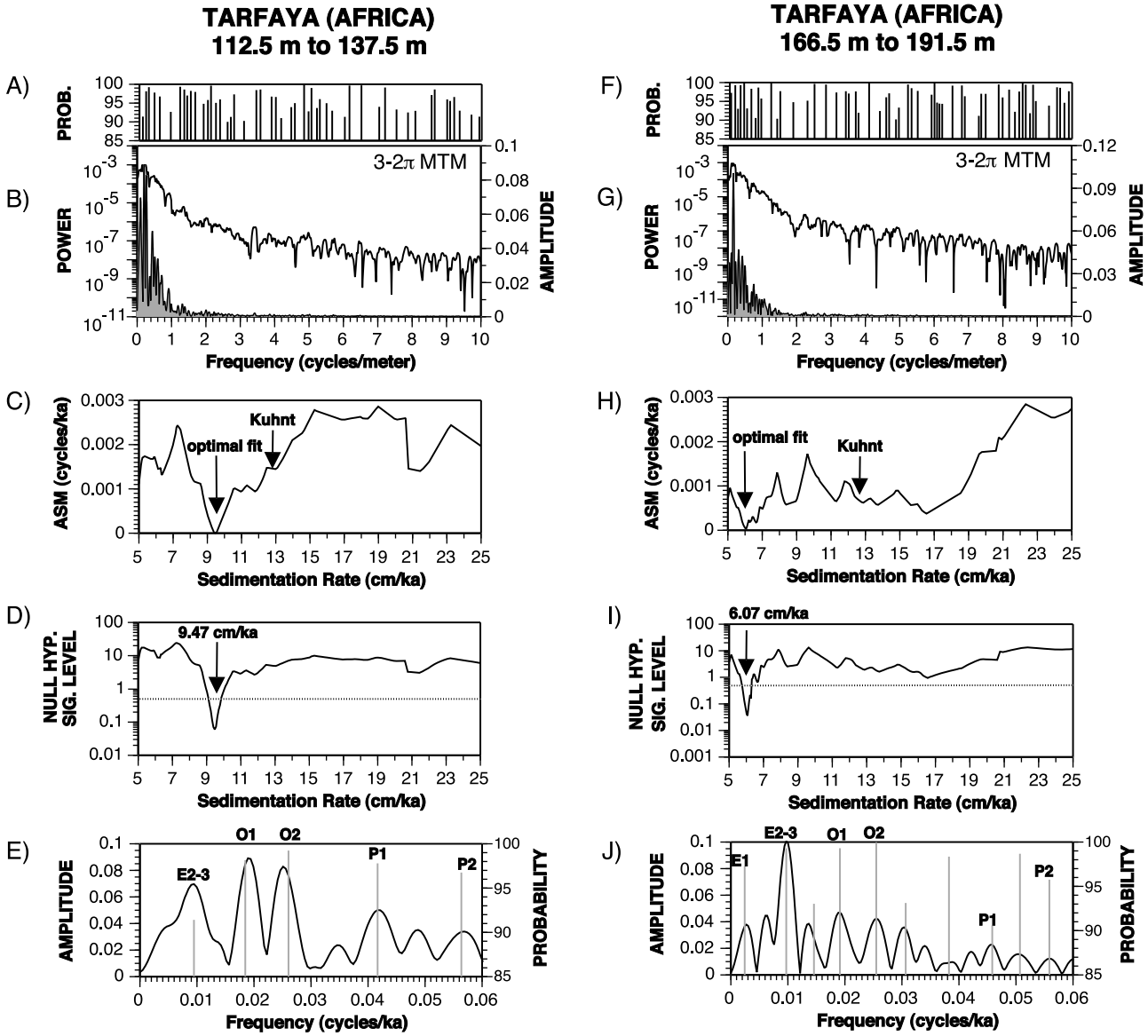

Figure 6. Multitaper method (MTM) spectral analyses and average spectral misfit (ASM) results for the Tarfaya S13 density data series. All MTM spectral analyses were conducted using three 2π tapers. ASM evaluates the astronomical model of *Laskar et al.* [2004, 2011], and is calculated for 200 individual sedimentation rates spanning 5 cm/ka to 25 cm/ka, with a logarithmic sedimentation rate scaling. (a) MTM harmonic analysis probability results for the data spanning 112.5–137.5 m. (b) Log MTM power spectrum estimate (bold line) and amplitude spectrum (gray) for the data spanning 112.5–137.5 m. (c) Average spectral misfit (in cycles/ka) for the data spanning 112.5–137.5 m. (d) Null hypothesis significance levels for the data spanning 112.5–137.5 m. The dotted line indicates a critical significance level of 0.5%. (e) Calibrated amplitude spectrum (black line) and harmonic analysis probability results (vertical lines) for the data spanning 112.5–137.5 m, using a sedimentation rate of 9.47 cm/ka. (f) MTM harmonic analysis probability results for the data spanning 166.5–191.5 m. (g) Log MTM power spectrum estimate (bold line) and amplitude spectrum (gray) for the data spanning 166.5–191.5 m. (h) Average spectral misfit (in cycles/ka) for the data spanning 166.5–191.5 m. (i) Null hypothesis significance levels for the data spanning 166.5–191.5 m. The dotted line indicates a critical significance level of 0.5%. (j) Calibrated amplitude spectrum (black line) and harmonic analysis probability results (vertical lines) for the data spanning 166.5–191.5 m, using a sedimentation rate of 6.07 cm/ka. In Figures 6c and 6h, "Kuhnt" indicates the sedimentation rate proposed by *Kuhnt et al.* [1997].

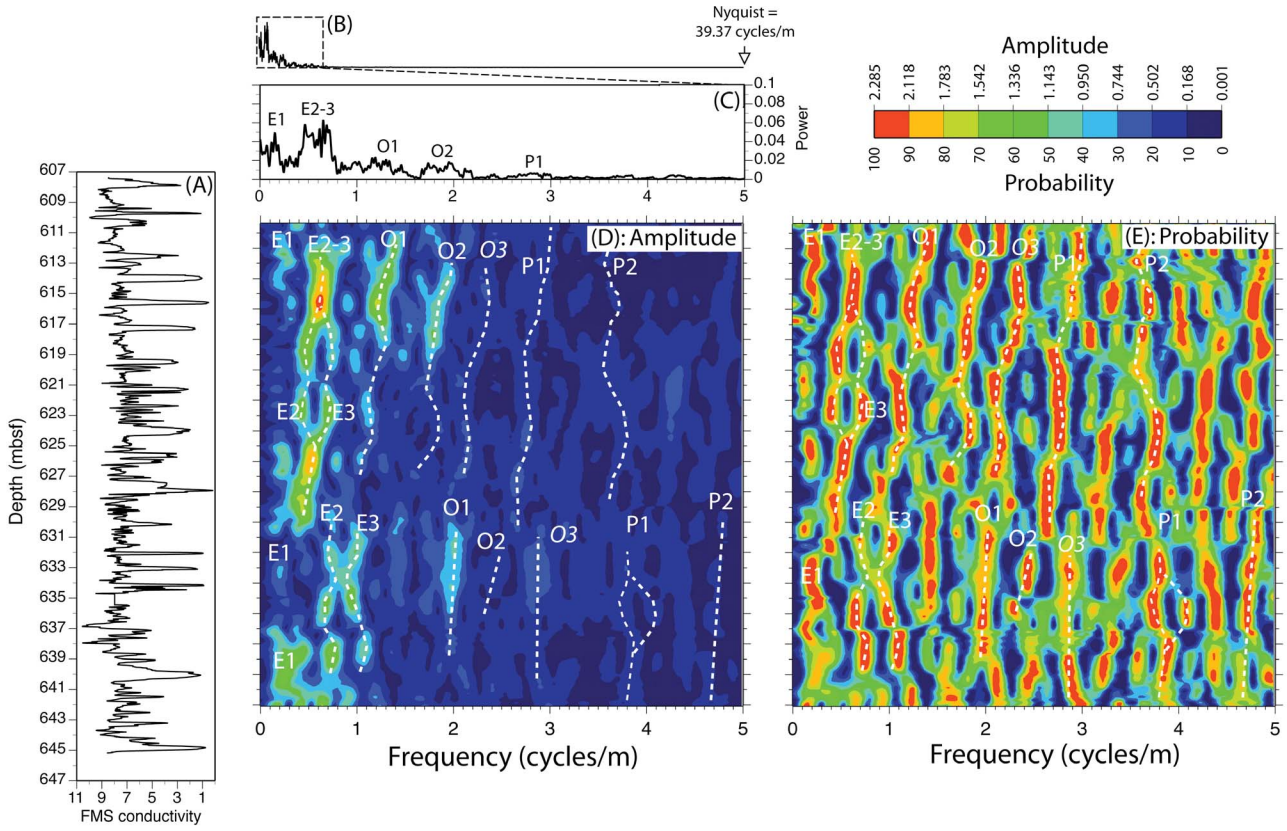

Figure 7. Time series analyses for ODP Site 1261B at Demerara Rise. (a) FMS conductivity data series for ODP Site 1261B [*Shipboard Scientific Party*, 2004]. (b) Three 2π taper MTM power spectrum of the entire FMS data series, plotted from 0 cycles/m to the Nyquist frequency of ~39.37 cycles/m. (c) Expanded view of this MTM power spectrum from 0 cycles/m to 5 cycles/m. (d) EHA amplitude results using three 2π tapers and an ~6-m moving window. (e) EHA probability results using three 2π tapers and an ~6-m moving window.

than half of the previously published astrochronologic estimate [*Kuypers et al.*, 2004], thus the ASM-derived short eccentricity and obliquity cycles were previously interpreted as obliquity and precession, respectively. In contrast to site 603B, the Moroccan coastal upwelling site (Tarfaya S13) reveals pronounced changes in bedding frequencies during and following the OAE 2 interval, diagnostic of sedimentation rate changes (Figure 5). Evolutive ASM analysis (Figure 6 and Figures S2 and S3) identifies substantially different sedimentation rates for the upper (post-OAE 2) and lower (OAE 2) portions of the record (125 m depth: 9.47 cm/ka, H_o-SL = 0.060%; 179 m depth: 6.07 cm/ka, H_o-SL = 0.036%). The 6.07 cm/ka sedimentation rate for the lower portion of this record (Figure 6i) is approximately half of the previous estimate [*Kuhnt et al.*, 1997], and – as was the case at DSDP 603B – indicates that the ASM-derived short eccentricity and obliquity cycles in this interval were previously interpreted as obliquity and precession, respectively.

[30] The FMS data series from Demerara Rise is somewhat noisier than the records from 603B and Tarfaya S13. Evolutive ASM analysis of this data series indicates substantial changes in bedding frequencies through the study interval (Figures 7 and 8; Figures S4 and S5). Similar to Tarfaya S13, the OAE 2 interval is characterized by a lower sedimentation rate (635.36 mbsf: 1.14 cm/ka, H_o-SL = 0.077%) than that of the post-OAE 2 interval (612.81 mbsf: 1.48 cm/ka, H_o-SL = 0.021%) (Figure 8).

[31] Calibration of the individual spectra using their ASM-derived sediment accumulation rates illustrates the eccentricity, obliquity and precession terms at each location (Figures 4e, 6e, 6j, 8e, and 8j; see also Tables S2–S11 in the auxiliary material). Using the new cyclostratigraphic calibrations, astronomical tuning is conducted to evaluate the duration of the OAE 2 carbon isotope excursion at Tarfaya and Demerara Rise (the two sites that unambiguously preserve the full event; details on the astronomical tuning procedures are contained in the auxiliary material). The duration of the excursion is dependent upon how the termination is defined [see, e.g., *Sageman et al.*, 2006], and further limitations are presented by the variable resolution of the carbon isotopic data, as well as the judgment of correlative features given the complexity of some records. In consideration of these factors, the amount of astronomical time between the excursion initiation and the "end of the plateau" (see auxiliary material) at Tarfaya is 450–500 ka, and the duration at Demerara Rise is 500–550 ka (Figure S6). These results compare reasonably well with the recently published

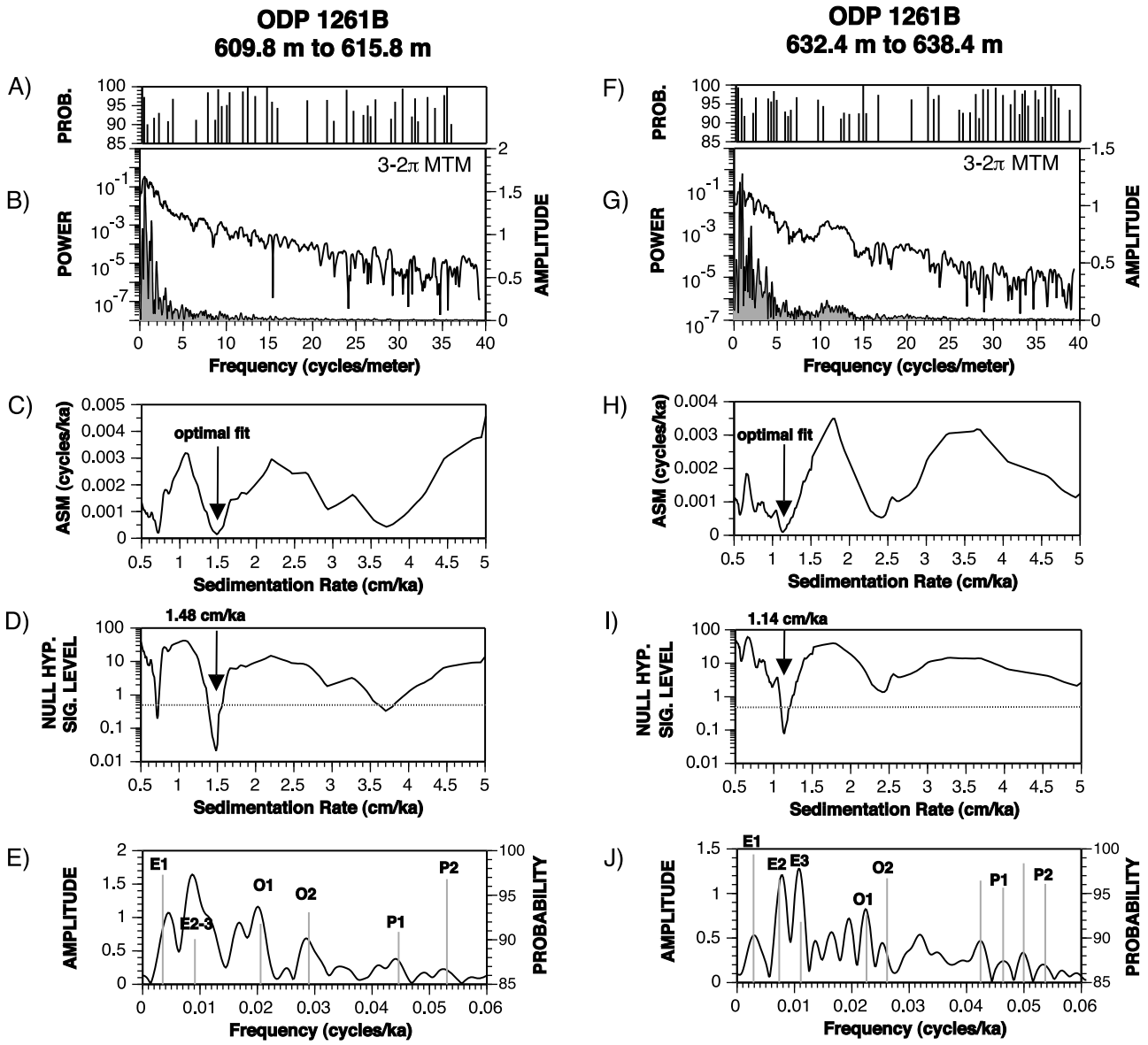

Figure 8. Multitaper method (MTM) spectral analyses and average spectral misfit (ASM) results for the ODP Site 1261B FMS conductivity data series. All MTM spectral analyses were conducted using three 2π tapers. ASM evaluates the astronomical model of *Laskar et al.* [2004, 2011], and is calculated for 200 individual sedimentation rates spanning 0.5 cm/ka to 5 cm/ka, with a logarithmic sedimentation rate scaling. (a) MTM harmonic analysis probability results for the data spanning 609.8–615.8 m. (b) Log MTM power spectrum estimate (bold line) and amplitude spectrum (gray) for the data spanning 609.8–615.8 m. (c) Average spectral misfit (in cycles/ka) for the data spanning 609.8–615.8 m. (d) Null hypothesis significance levels for the data spanning 609.8–615.8 m. The dotted line indicates a critical significance level of 0.5%. (e) Calibrated amplitude spectrum (black line) and harmonic analysis probability results (vertical lines) for the data spanning 609.8–615.8 m, using a sedimentation rate of 1.48 cm/ka. (f) MTM harmonic analysis probability results for the data spanning 632.4–638.4 m. (g) Log MTM power spectrum estimate (bold line) and amplitude spectrum (gray) for the data spanning 632.4–638.4 m. (h) Average spectral misfit (in cycles/ka) for the data spanning 632.4–638.4 m. (i) Null hypothesis significance levels for the data spanning 632.4–638.4 m. The dotted line indicates a critical significance level of 0.5%. (j) Calibrated amplitude spectrum (black line) and harmonic analysis probability results (vertical lines) for the data spanning 632.4–638.4 m, using a sedimentation rate of 1.14 cm/ka.

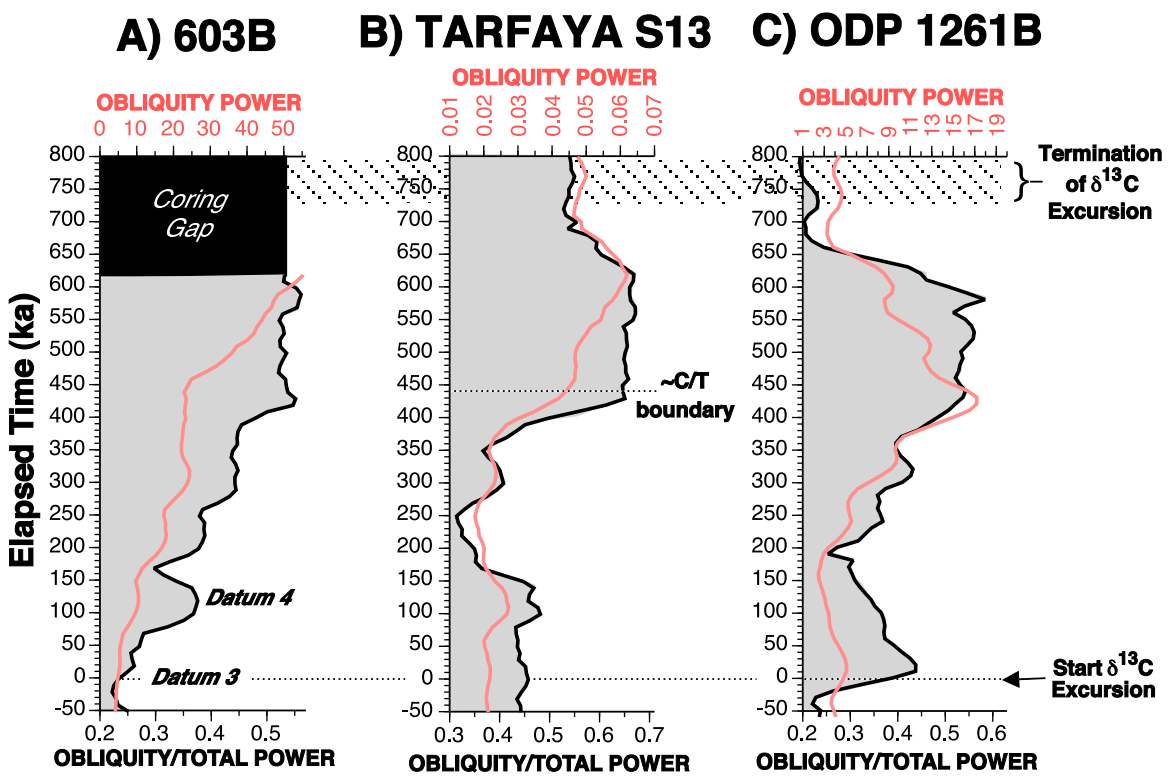

Figure 9. (a) Temporal changes in obliquity forcing at DSDP 603B. "Datum 3" and "Datum 4" refer to the $\delta^{13}C_{phytane}$ data [*Kuypers et al.*, 2004] identified in Figure 2a. (b) Temporal changes in obliquity forcing at Tarfaya S13. (c) Temporal changes in obliquity forcing at Demerara Rise ODP 1261B. Red lines indicate total power in the obliquity band (0.015–0.04 cycles/ka), and the black lines indicate the fraction of the power in the obliquity band, as compared to total power at frequencies less than 1/10,000 years. Analyses were conducted using 2π MTM power spectra (three data tapers) and a 300 ka moving window.

radioisotopic/astrochronologic time scale at the Cenomanian-Turonian GSSP [*Meyers et al.*, 2012; *Sageman et al.*, 2006], which indicates a duration between 520 and 560 ka to the "end of the plateau" (the C/T boundary).

5. Discussion

5.1. An Evaluation of Changes in Orbital Forcing During OAE 2

[32] Having tested for the presence of orbital influence independently at each location, and quantitatively identified the astronomical signal, it is possible to evaluate the interaction between longer-term secular changes in climate (potentially due to OAE 2) and shorter-term orbital forcing. Our assessment is conducted by performing an MTM evolutive power spectral analysis on the astronomically tuned data series, followed by integration of the spectrum over the frequency bands of interest. Analysis of the wt.% TOC data from DSDP 603B reveals a progressive amplification of obliquity forcing during OAE 2 at this midlatitude deep ocean site (Figure 9a). The astronomically tuned data series from the near-equatorial coastal upwelling sites (Tarfaya S13 and ODP 1261B) also reveal obliquity amplification (Figures 9b and 9c), although the onset at Tarfaya appears to be delayed by at least 250,000 years, likely indicative of a regional overprint.

[33] The marked change in strength of the obliquity signal in both midlatitude deep ocean and shallow tropical shelf environments suggests the existence of a high-latitude teleconnection that is sensitive to orbital-insolation. The observed obliquity signal could be attributable to high latitude intermediate/deep-water formation. For example, orbital forcing of high-latitude temperature and/or precipitation could affect the rate of intermediate/deep-water formation and thus oxygen availability at DSDP 603B, controlling the development of the organic-carbon rich/poor couplets (a ventilation cycle). In principle, such ventilation cycles could influence the tropical shelf settings as well [see also *Nederbragt et al.*, 2007; *Friedrich et al.*, 2008b; *Jiménez Berrocoso et al.*, 2008; *März et al.*, 2009]. If obliquity-forced temperature changes were the important factor modulating high-latitude intermediate/deep-water formation, they could have also exerted control on low-latitude wind strength via the meridional temperature gradient [*Kuhnt et al.*, 1997], affecting upwelling and productivity at Tarfaya and Demerara Rise. Alternatively, the observed obliquity signal could be the consequence of enhanced polar glaciation [*Bornemann et al.*, 2008; *Gale et al.*, 2008] and associated glacio-eustatic responses, although numerous studies have challenged the existence of polar ice sheets during the late

Cretaceous [e.g., *Huber et al.*, 2002; *Moriya et al.*, 2007; *Ando et al.*, 2009].

[34] While the observation of a dominant obliquity signal at these three sites is difficult to explain without a sensitive high-latitude teleconnection during the late Cretaceous, the progressive amplification of obliquity power may arise via two distinct processes. Foremost, the obliquity amplification could be partially or wholly attributable to an increase of obliquity influence on orbital-insolation, which is characterized by a quasiperiodic 1.2 Ma amplitude modulation [*Laskar et al.*, 2004]. Alternatively, the obliquity amplification could be due to the progressive development of a high-latitude climate system component that is sensitive to obliquity forcing during OAE 2, irrespective of the theoretical 1.2 Ma amplitude modulation.

[35] Unfortunately, a direct quantification of obliquity amplitude modulations in the theoretical astronomical solution of *Laskar et al.* [2004] is not strictly valid beyond 40–50 Ma, due to uncertainties in the model. Despite this limitation, *Mitchell et al.* [2008] propose that OAE 2 is associated with a simultaneous node (minimum in amplitude) in obliquity and eccentricity that is observed at ~93.9 Ma in the *Laskar et al.* [2004] model. Relevant to this issue, recent recalibration of the C/T boundary [*Meyers et al.*, 2012] has shifted the OAE 2 interval 0.35 Ma older than previously estimated [*Sageman et al.*, 2006]. This now places the initiation of OAE 2 at a time of maximum obliquity power in the theoretical *Laskar et al.* [2004] model, with minimum values coinciding with the C/T boundary (near the end of OAE 2); this is the opposite of what our analysis has shown for site 603B, Demerara Rise and Tarfaya (Figure 9). If the obliquity amplification documented at these three sites accurately reflects primary changes in orbital-insolation – rather than the independent development of a new high latitude climate system component – it provides an important tuning constraint for future astrodynamical modeling, and is also consistent with the presence of an obliquity node near the initiation of OAE 2.

[36] It is not yet possible to quantitatively deconvolve the relative roles of the two potential sources of obliquity amplification outlined above, and both may be important factors during OAE 2. However, the observation of strong obliquity power clearly implicates a high-latitude teleconnection, and the amplification of obliquity is intimately linked to the OAE 2. The later point is illustrated by the close relationship between obliquity amplification, the carbon isotope excursion and Nd-isotope excursion (discussed further below) documented at Demerara Rise, all of which initiate and terminate in unison (see section 5.2; Figure 10). Thus, these results suggest that the proto-North Atlantic was strongly sensitive to a high-latitude climate system component during OAE 2, and that this high-latitude forcing was the dominant factor pacing organic matter accumulation by the latter portion of OAE 2, and possibly earlier.

5.2. Implications of the Obliquity Amplification for OAE 2

[37] How does the identification of obliquity amplification inform our understanding of the oceanographic mechanisms that ultimately generated the OAE 2? Osmium isotope analyses spanning OAE 2 at Demerara Rise [*Turgeon and Creaser*, 2008] demonstrate a marked shift to values typical of a magmatic source just prior to the positive carbon isotope excursion (Figure 10a). This observation is consistent with the hypothesis that a pulse of magmatism is the underlying trigger for the development of OAE 2 [*Sinton and Duncan*, 1997; *Jones and Jenkyns*, 2001; *Snow et al.*, 2005; *Turgeon and Creaser*, 2008; *Adams et al.*, 2010]. εNd data from Demerara Rise [*MacLeod et al.*, 2008; *Martin et al.*, 2012] also display a pronounced excursion, and the directionality is compatible with an enhanced magmatic source; however, *Martin et al.* [2012] have demonstrated that this is an unlikely mechanism for producing the observed ϵNd excursion.

[38] Instead, the εNd excursion most likely indicates a new source of intermediate water bathing Demerara Rise during OAE 2 [*MacLeod et al.*, 2008; *Martin et al.*, 2012]. Given that obliquity forcing dominates high-latitude insolation changes, a reorganization of intermediate/deep water formation from lower to higher latitude is consistent with the amplification of obliquity observed across deep ocean to shelf settings in the proto-North Atlantic (Figures 9 and 10d). Lending support to this hypothesis, the ϵNd values at Demerara Rise before and after OAE 2 are compatible with a low-latitude intermediate water source on the South American craton [*MacLeod et al.*, 2008; *Martin et al.*, 2012], while the values during OAE 2 require an alternative source region. Furthermore, detailed comparison of the pattern of obliquity amplification and the Nd-isotope record from Site 1261 (Figures 10d and 10e) [*Martin et al.*, 2012] reveals much similarity, with the exception of a large discrepancy at ~250,000 years. Here, a Nd-isotope maximum is observed without a contemporaneous obliquity amplification maximum. The discrepancy is potentially an artifact of interpolation across intercalated volcanic ashes at this stratigraphic level (see Figure S6), which would serve to locally diminish the obliquity power at Site 1261. If this is the case, a simplistic interpretation of the obliquity amplification is that it reflects a mixing ratio of two distinct water masses, one of which is local, and the other derived from high-latitude. Regardless of the source regions, the wide range of Nd-isotope values observed during OAE 2 suggest variable mixing of water masses.

[39] Considering the paleogeography of the late Cenomanian and the semi-closed nature of the proto-North Atlantic, sources for an alternate intermediate water mass include the Pacific (via the Central American Seaway) [*Trabucho Alexandre et al.*, 2010], the circum-North Atlantic region (including the western European shelf seas) [*Voigt et al.*, 2004], the southern Tethys [*Jiménez Berrocoso et al.*, 2010], and the Western Interior Seaway [*Hay et al.*, 1993]. The existence of a large regional sill (the Walvis Ridge) likely limited intermediate water flow between the proto-South and proto-North Atlantic [*Friedrich et al.*, 2012]. ϵNd data from both the Pacific and southern Tethys are compatible with the Nd-isotope signature observed at Demerara Rise during OAE 2, but available data from the western European shelf suggests that this location can be excluded [*MacLeod et al.*, 2008; *Trabucho Alexandre et al.*, 2010; *Jiménez Berrocoso et al.*, 2010; *Martin et al.*, 2012]. While there exists some uncertainty about the depth and width of the Central American Seaway, and thus its ability to exchange intermediate water from the Pacific [*Hay*, 1999; *Trabucho Alexandre et al.*, 2010], it has been suggested that the spatial patterns of εNd data in the proto-North Atlantic support a

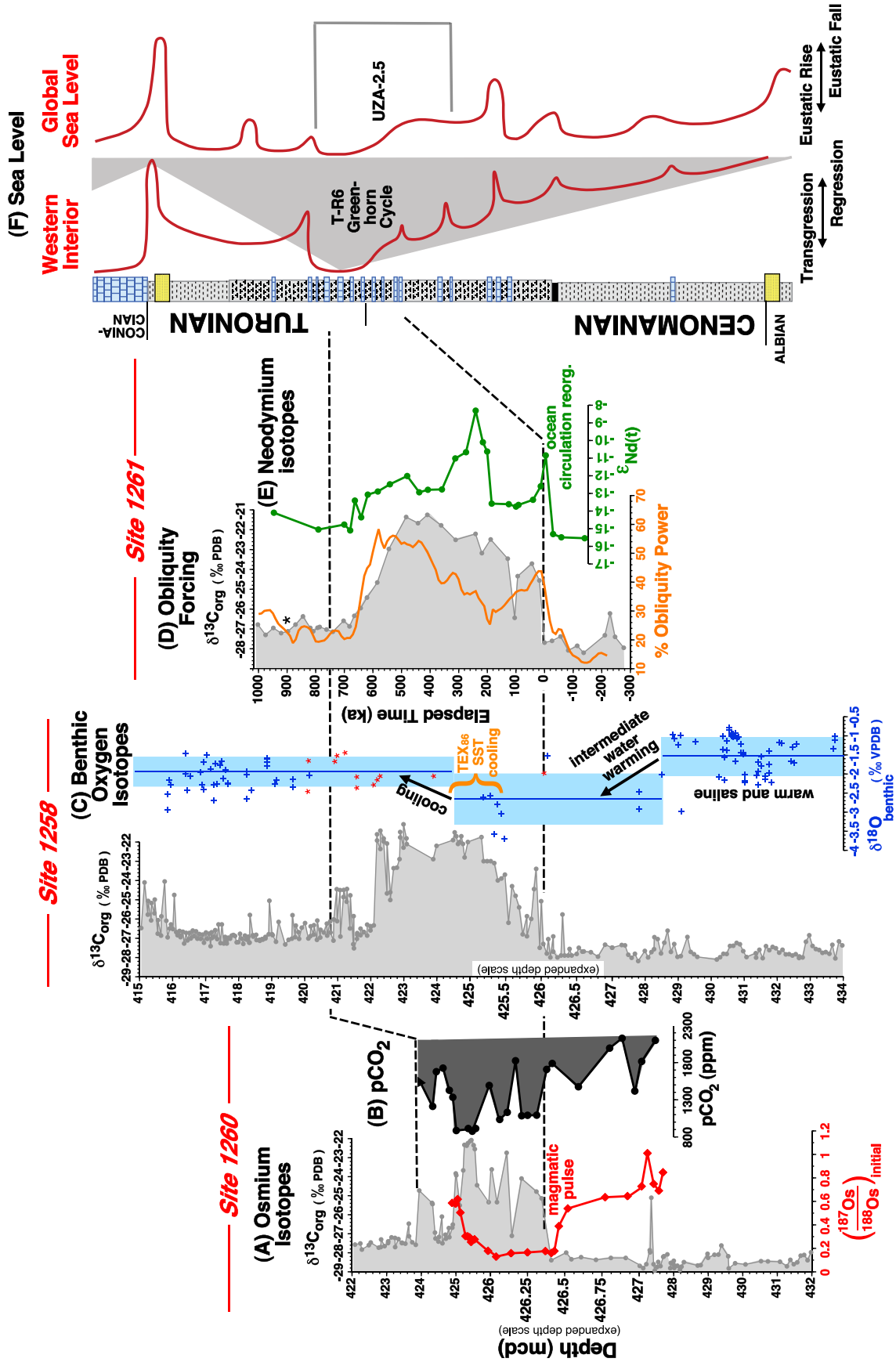
(F) Sea Level
Global Sea Level
Western Interior
UZA-2.5
T-R6 Green-horn Cycle
Eustatic Rise
Eustatic Fall
Transgression
Regression
CONIA-CIAN
TURONIAN
CENOMANIAN
ALBIAN
Site 1261
(E) Neodymium isotopes
ocean circulation reorg.
εNd(t)
(D) Obliquity Forcing
δ13Corg (‰ PDB)
% Obliquity Power
Elapsed Time (ka)
Site 1258
(C) Benthic Oxygen Isotopes
cooling
TEX86 SST cooling
intermediate water warming
warm and saline
δ18Obenthic (‰ VPDB)
δ13Corg (‰ PDB)
(expanded depth scale)
Site 1260
(A) Osmium Isotopes
(B) pCO2
pCO2 (ppm)
magmatic pulse
(187Os/188Os)initial
Depth (mcd)
(expanded depth scale)

Figure 10

deep connection during OAE 2 [*Martin et al.*, 2012]. The southern Tethys would appear a less likely source due to its low latitude, which is inconsistent with the strong obliquity amplification that we observe across deep ocean to shelf settings during the event.

[40] The final potential source region for intermediate/deep water is the Western Interior Seaway (WIS), an inference that is supported by εNd data from both bulk marlstone (G. L. Farmer, personal communication, 2009) and molluscan shell material [*Whittaker and Kyser*, 1993] that yield values of approximately −6 (compare this to the maximum ϵNd observed at Demerara Rise during OAE 2 of −7) [*Martin et al.*, 2012]. Furthermore, benthic foraminifera oxygen isotopic data from the OAE 2 interval in the northern WIS are consistent with a water mass density (σ_t) of approximately 24.5 (assuming $\delta_w = -3.38$ permil) [*Fisher and Arthur*, 2002], substantially greater than estimates of 20–21 for tropical surface water from the Demerara Rise [*Voigt et al.*, 2004]. Assuming that the buoyancy flux of this water mass was adequate, this indicates the plausibility of a WIS source for Demerara Rise intermediate water.

[41] Thus, we propose a conceptual model for OAE 2 in which a change in intermediate/deep water mass source from lower to higher latitude occurred, driven by the achievement of a critical sea level rise [*Haq et al.*, 1987; *Sageman et al.*, 1997; *Arthur and Sageman*, 2005] (Figure 10f) that created expanses of high latitude shallow seaways, prone to the development of dense water masses [*Hay et al.*, 1993; *Voigt et al.*, 2004]. If the WIS is the source region, intensification of the intermediate/deep water production would have progressed as sea level rise inundated greater areas of mid to high latitude shelf [*Arthur et al.*, 1987; *Hay et al.* 1993], potentially augmented by episodic climatic cooling associated with enhanced organic matter burial, and modulated by obliquity-forced salinity/temperature influence on surface water density. This model is consistent with the physical oceanographic analysis of *Hay et al.* [1993], which concluded that mixing (caballing) of southern and northern water masses in the WIS may have generated an intermediate water mass for the world ocean, with maximum production during times of maximum transgression, that is, during OAE 2. The observation of a strong obliquity signal expressed in late Cenomanian/early Turonian deposits from the central WIS (the Bridge Creek Limestone Member) [*Sageman et al.*, 1997, 1998; *Meyers et al.*, 2001] also lends support to an obliquity influence on surface water density and intermediate/deep water production.

[42] It has been widely noted that portions of the restricted proto-North Atlantic display an onset of organic carbon-rich deposition well before the initiation of OAE 2 [e.g., *Arthur et al.*, 1987; *Trabucho Alexandre et al.*, 2010; *Jiménez Berrocoso et al.*, 2010], suggestive of a regional suboxic/anoxic water layer that pre-dated the global event. The addition of hydrothermally derived trace elements and reduced compounds via enhanced magmatism would have augmented the nutrient supply in this relatively deep water mass, and further diminished its oxygen content [*Sinton and Duncan*, 1997; *Turgeon and Creaser*, 2008; *Adams et al.*, 2010]. We hypothesize that a denser water mass derived from the high latitudes displaced this nutrient-rich anoxic layer during OAE 2. The scenario provides a new mechanism for the two phase OAE 2 model introduced by *Turgeon and Creaser* [2008], where an initial increase in organic carbon burial from magmatism-enhanced bottom water oxygen depletion is later followed by a breakdown in ocean stratification, stimulating surface ocean primary productivity.

5.3. Comparison With Temperature Proxy Estimates

[43] OAE 2 occurred during a time of peak climatic warmth known as the "mid-Cretaceous climate optimum" [*Norris et al.*, 2001; *Friedrich et al.*, 2012]. In detail, temperature proxy reconstructions indicate warming just prior to and/or throughout much of OAE 2 [e.g., *Clarke and Jenkyns*, 1999; *Huber et al.*, 2002; *Voigt et al.*, 2004; *Jenkyns et al.*, 2004, *Kuhnt et al.*, 2005; *Voigt et al.*, 2006; *Forster et al.*, 2007a, 2007b; *Friedrich et al.*, 2008a], with one or more transient cooling events in some locations [e.g., *Voigt et al.*, 2006; *Forster et al.*, 2007a, 2007b; *Sinninghe Damsté et al.*, 2010]. The Demerara Rise record provides a particularly intriguing perspective on the evolution of ocean temperature during OAE 2. While benthic foraminifera oxygen isotope data is compatible with warming just prior to OAE 2 (interval "4" of *Friedrich et al.* [2008a]), this is followed by a shift to heavier $\delta^{18}O$ values in the early phase of OAE 2 (the base of interval "5" of *Friedrich et al.* [2008a]), consistent with an interpretation of sustained intermediate water cooling (Figure 10c). In contrast, sea surface temperature estimates at Demerara Rise using the TEX_{86} proxy method [*Forster et al.*, 2007a, 2007b] suggest high surface ocean temperatures that persisted into the middle Turonian, with a transient cooling

Figure 10. Summary of key OAE 2 data from Demerara Rise. The dashed lines identify two correlative horizons based upon nannofossil biostratigraphy [*Hardas and Mutterlose*, 2006] and carbon isotope data [*Erbacher et al.*, 2005; *Friedrich et al.*, 2008a]. A more detailed correlation of these $\delta^{13}C_{org}$ data has been conducted in some studies, but is not implied here. An alternative correlation point for site 1261 is indicated by the black asterisk in panel D (at ~900 ka). (a) Initial seawater $^{187}Os/^{188}Os$ (red diamonds) [*Turgeon and Creaser*, 2008] for Site 1260. Depth scale between 426 and 427 m is expanded. (b) The atmospheric pCO_2 reconstruction of *van Bentum et al.* [2012] for site 1260 (black circles). (c) Benthic foraminifera $\delta^{18}O$ data from Site 1258 (blue crosses) [*Friedrich et al.*, 2008a]. The approximate location of benthic foraminifera $\delta^{18}O$ data from Site 1260 is also indicated with red asterisks [*Friedrich et al.*, 2008a]. Dark blue lines indicate interval mean values (based on data from Site 1258 and 1260) and light blue fields capture 90% of the $\delta^{18}O$ data in each interval [*Friedrich et al.*, 2008a]. The approximate location of the TEX_{86} SST cooling event (observed at Site 1260) is based on the inter-site correlation presented in *Friedrich et al.* [2008a]. Depth scale between 425 and 427 m is expanded. (d) Temporal changes in obliquity forcing at Site 1261, measured as a percentage of total FMS data variance (at periods > 10,000 years) (brown line), and orbitally tuned $\delta^{13}C_{org}$ data (gray circles [*Erbacher et al.*, 2005]) for Site 1261. (e) Orbitally tuned fish debris ϵNd(t) data (green dots [*Martin et al.*, 2012]) for Site 1261. (f) Lithostratigraphy of the Greenhorn marine cycle of the Cretaceous Western Interior Basin (USA) [*Sageman et al.*, 1997], reconstructed sea level history within the basin [*Sageman et al.*, 1997], and global sea level [*Haq et al.*, 1987] (after *Sageman et al.* [1997]).

event at the beginning of OAE 2 (Figure 10c). TEX_{86} paleotemperature reconstructions from the eastern equatorial Atlantic (DSDP Site 367) [*Forster et al.*, 2007a] and northwest Atlantic (ODP Site 1276) [*Sinninghe Damsté et al.*, 2010] also document this transient cooling event. While the decoupling of surface and intermediate water temperature proxy records at Demerara Rise could be due to issues associated with the proxy reconstructions [e.g., *Shah et al.*, 2008] including changes in salinity [*Friedrich et al.*, 2008a], the results are also compatible with a complex oceanographic response to OAE 2. The discrepancy between surface and intermediate water paleotemperature changes may reflect a precariously balanced oceanic stratification that was susceptible to a major reorganization.

5.4. Linkages Between Eustacy, Magmatism, and Oceanographic Response During OAE 2

[44] The scenario outlined in sections 5.2–5.3 provides a further mechanism for the development of OAE 2 that could have augmented processes related to increased magmatism that have been proposed by *Sinton and Duncan* [1997], *Kerr* [1998, 2005], *Turgeon and Creaser* [2008], *Adams et al.* [2010] and others. In accord with the *Turgeon and Creaser* [2008] model, the disparity between surface water and intermediate water temperature changes observed at Demerara Rise [*Forster et al.*, 2007a; *Friedrich et al.*, 2008a], particularly the transient SST cooling event near the beginning of OAE 2, could be the consequence of a transitional "destratification" period during which a high-latitude intermediate/deep water source became established; the mixing of "warm" (<30°C) [*Friedrich et al.*, 2008a] intermediate water into the surface ocean would result in the observed intermittent cooling (between 31 and 37°C, dependent upon the temperature calibration) [*Forster et al.*, 2007a; *Sinninghe Damsté et al.*, 2010]. Importantly, ocean stagnation provides a strong barrier to the development of widespread anoxia and euxinia [*Shen et al.*, 2002; *Meyer and Kump*, 2008; *Kump et al.*, 2008], thus the reorganization (and potential invigoration) of ocean circulation may have been a critical step in the establishment of OAE 2.

[45] Finally, *Sageman et al.* [1997] hypothesize a link between organic matter burial, CO_2 drawdown, cooling and obliquity amplification during OAE 2. A number of atmospheric pCO_2 estimates across the OAE 2 interval have been proposed [*Freeman and Hayes*, 1992; *Kuypers et al.*, 1999; *Bice et al.*, 2006; *Barclay et al.*, 2010; *Sinninghe Damsté et al.*, 2008, 2010; *Jarvis et al.*, 2011; *van Bentum et al.*, 2012], all of which confirm atmospheric CO_2 drawdown, but with important discrepancies in magnitude and/or timing of the reduction. Only a few of the reported pCO_2 estimates span the entire OAE 2 interval in detail [e.g., *Freeman and Hayes*, 1992; *Jarvis et al.*, 2011; *van Bentum et al.*, 2012]. The most recent of these estimates – a reconstruction from Demerara Rise [*van Bentum et al.*, 2012] (Figure 10b) – indicates minimum pCO_2 during the latter portion of OAE 2, at a time of sustained high sea surface temperatures as ascertained by TEX_{86} data. This is also the time of maximum obliquity amplification at Demerara Rise (Figure 10d). Taking the pCO_2 and TEX_{86} results at face value, the SST cooling hypothesized by *Sageman et al.* [1997] would be most obvious at the high latitudes where the impact of atmospheric carbon dioxide on temperature is more pronounced, and thus more clearly resolvable given the stated accuracy and precision of the TEX_{86} method [*Kim et al.*, 2008; *Liu et al.*, 2009; *Sinninghe Damsté et al.*, 2010]. High-latitude TEX_{86} SST estimates are not yet available for the OAE 2, but this provides a testable hypothesis for future work. Independent of temperature influences, obliquity amplification during OAE 2 can be readily ascribed to increases in intermediate water production in the WIS, associated with the largest transgression of the Mesozoic [*Haq et al.*, 1987; *Hay et al.*, 1993].

[46] Interestingly, *Westerhold and Röhl* [2009] also identify a transient (~700 ka) amplification of obliquity influence at Demerara Rise from 50.1 to 49.4 Ma. This interval coincides with the onset of long-term Cenozoic cooling and also appears to be associated with a substantial drop in atmospheric pCO_2 [*Westerhold and Röhl*, 2009], suggesting that Demerara Rise was particularly sensitive to such climate transitions. Our new results suggest a complex interaction between long-term tectono-eustatic sea level rise, major magmatic events, and changes in ocean circulation, which ultimately had a profound impact on Late Cretaceous biogeochemistry and climate.

[47] **Acknowledgments.** This study was supported by National Science Foundation grants EAR-0001093 (B.B.S.) and EAR-0959108 (S.R.M. and B.B.S.) and the Yale Institute for Biospheric Studies Gaylord Donnelley Environmental Fellowship (S.R.M.). We thank Wolfgang Kuhnt (University of Kiel) for providing new density log data from the Tarfaya S13 core. A digital version of the $\delta^{13}C_{org}$ data for the Tarfaya S13 core was kindly provided by Thomas Wagner (University of Newcastle). S.R.M. thanks Robert Locklair for insights on analysis of the ODP 1261B FMS data series. Graham Weedon, Alberto Malinverno, and an anonymous reviewer provided comments that substantially improved the manuscript.

References

Adams, D. D., M. T. Hurtgen, and B. B. Sageman (2010), Volcanic triggering of a biogeochemical cascade during Oceanic Anoxic Event 2, *Nat. Geosci.*, *3*, 201–204, doi:10.1038/ngeo743.

Ando, A., B. Huber, K. MacLeod, T. Ohta, and B.-K. Khim (2009), Blake Nose stable isotopic evidence against the mid-Cenomanian glaciation hypothesis, *Geology*, *37*, 451–454, doi:10.1130/G25580A.1.

Arthur, M. A., and B. B. Sageman (2005), Sea level control on source rock development: Perspectives from the Holocene Black Sea, the mid-Cretaceous Western Interior Basin of North America, and the Late Devonian Appalachian Basin, in *The Deposition of Organic Carbon-Rich Sediments: Models, Mechanisms and Consequences*, edited by N. B. Harris, *Spec. Publ. SEPM Soc. Sediment. Geol.*, *82*, 35–59.

Arthur, M. A., S. O. Schlanger, and H. C. Jenkyns (1987), The Cenomanian-Turonian ocean anoxic event, II. Palaeoceanographic controls on organic-matter production and preservation, in *Marine Petroleum Source Rocks*, edited by J. Brooks and A. Fleet, *Geol. Soc. London Spec. Publ.*, *26*, 401–420.

Barclay, R. S., J. C. McElwain, and B. B. Sageman (2010), Carbon sequestration activated by a volcanic CO_2 pulse during Oceanic Anoxic Event 2, *Nat. Geosci.*, *3*, 205–208, doi:10.1038/ngeo757.

Berger, A., M. F. Loutre, and J. Laskar (1992), Stability of the astronomical frequencies over the Earth's history for paleoclimate studies, *Science*, *255*, 560–566, doi:10.1126/science.255.5044.560.

Bice, K. L., D. Birgel, P. A. Meyers, K. A. Dahl, K.-U. Hinrichs, and R. D. Norris (2006), A multiple proxy and model study of Cretaceous upper ocean temperatures and atmospheric CO_2 concentrations, *Paleoceanography*, *21*, PA2002, doi:10.1029/2005PA001203.

Bornemann, A., R. D. Norris, O. Friedrich, B. Beckmann, S. Schouten, J. S. Sinninghe Damsté, J. Vogel, P. Hoffmann, and T. Wagner (2008), Isotopic evidence for glaciation during the Cretaceous supergreenhouse, *Science*, *319*, 189–192, doi:10.1126/science.1148777.

Clarke, L. J., and H. C. Jenkyns (1999), New oxygen isotope evidence for long-term Cretaceous climatic change in the Southern Hemisphere, *Geology*, *27*, 699–702, doi:10.1130/0091-7613(1999)027<0699:NOIEFL>2.3.CO;2.

Einsele, G., and J. Wiedmann (1982), Turonian black shales in the Moroccan coastal basins: First upwelling in the Atlantic Ocean?, in *Geology of*

the Northwest African Continental Margin, edited by U. von Rad et al., pp. 396–414, Springer, Berlin, doi:10.1007/978-3-642-68409-8_16.

Erbacher, J., O. Friedrich, P. A. Wilson, H. Birch, and J. Mutterlose (2005), Stable organic carbon isotope stratigraphy across Oceanic Anoxic Event 2 of Demerara Rise, western tropical Atlantic, *Geochem. Geophys. Geosyst.*, *6*, Q06010, doi:10.1029/2004GC000850.

Fisher, C. G., and M. A. Arthur (2002), Water mass characteristics in the Cenomanian US Western Interior seaway as indicated by stable isotopes of calcareous organisms, *Palaeogeogr. Palaeoclimatol. Palaeoecol.*, *188*, 189–213, doi:10.1016/S0031-0182(02)00552-7.

Forster, A., S. Schouten, K. Moriya, P. A. Wilson, and J. S. Sinninghe Damsté (2007a), Tropical warming and intermittent cooling during the Cenomanian/Turonian oceanic anoxic event 2: Sea surface temperature records from the equatorial Atlantic, *Paleoceanography*, *22*, PA1219, doi:10.1029/2006PA001349.

Forster, A., S. Schouten, M. Baas, and J. S. Sinninghe Damsté (2007b), Mid-Cretaceous (Albian-Santonian) sea surface temperature record of the tropical Atlantic Ocean, *Geology*, *35*, 919–922, doi:10.1130/G23874A.1.

Freeman, K. H., and J. M. Hayes (1992), Fractionation of carbon isotopes by phytoplankton and estimates of ancient CO_2 levels, *Global Biogeochem. Cycles*, *6*, 185–198, doi:10.1029/92GB00190.

Friedrich, O., J. Erbacher, K. Moriya, P. Wilson, and H. Kuhnert (2008a), Warm saline intermediate waters in the Cretaceous tropical Atlantic Ocean, *Nat. Geosci.*, *1*, 453–457, doi:10.1038/ngeo217.

Friedrich, O., R. D. Norris, A. Bornemann, B. Beckmann, H. Palike, P. Worstell, P. Hofmann, and T. Wagner (2008b), Cyclic changes in Turonian to Coniacian planktic foraminiferal assemblages from the tropical Atlantic Ocean, *Mar. Micropaleontol.*, *68*, 299–313, doi:10.1016/j.marmicro.2008.06.003.

Friedrich, O., R. D. Norris, and J. Erbacher (2012), Evolution of middle to Late Cretaceous oceans - A 55 m.y. record of Earth's temperature and carbon cycle, *Geology*, *40*, 107–110, doi:10.1130/G32701.1.

Gale, A. S. (1995), Cyclostratigraphy and correlation of the Cenomanian Stage in western Europe, in *Orbital Forcing Timescales and Cyclostratigraphy*, edited by M. R. House and A. S. Gale, *Geol. Soc. Spec. Publ.*, *85*, 177–197, doi:10.1144/GSL.SP.1995.085.01.11.

Gale, A., S. Voigt, B. Sageman, and W. J. Kennedy (2008), Eustatic sea-level record for the Cenomanian (Late Cretaceous)- Extension to the Western Interior Basin, USA, *Geology*, *36*, 859–862, doi:10.1130/G24838A.1.

Haq, B. U., J. Hardenbol, and P. R. Vail (1987), Chronology of fluctuating sea levels since the Triassic (250 million years ago to present), *Science*, *235*, 1159–1167.

Hardas, P., and J. Mutterlose (2006), Calcareous nannofossil biostratigraphy of the Cenomanian/Turonian boundary interval of ODP Leg 207 at the Demerara Rise, *Rev. Micropaleontol.*, *49*, 165–179, doi:10.1016/j.revmic.2006.04.005.

Hay, W. W. (1999), An alternative global Cretaceous paleogeography, in *Evolution of the Cretaceous Ocean/Climate System*, edited by E. Barrera and C. Johnson, *Spec. Pap. Geol. Soc. Am.*, *332*, 1–47.

Hay, W. W., D. L. Eicher, and R. Diner (1993), Physical oceanography and water masses in the Western Interior Seaway, in *Evolution of the Western Interior Basin*, edited by W. G. E. Caldwell and E. G. Kauffman, *Geol. Assoc. Can. Spec. Pap.*, *39*, 297–318.

Hays, J. D., J. Imbrie, and N. J. Shackleton (1976), Variations in the Earth's orbit: Pacemaker of the ice ages, *Science*, *194*, 1121–1132, doi:10.1126/science.194.4270.1121.

Herbert, T. D. (1994), Reading orbital signals distorted by sedimentation: Models and examples, in *Orbital Forcing and Cyclic Sequences*, edited by P. L. de Boer and D. G. Smith, *Spec. Publ. Int. Assoc. Sedimentol.*, *19*, 483–507.

Herbin, J. P., E. Masure, and J. Roucache (1987), Cretaceous formations from the lower continental rise off Cape Hatteras: Organic geochemistry, dinoflagellate cysts, and the Cenomanian/Turonian boundary event at Sites 603(Leg 93) and 105(Leg 11), *Initial Rep. Deep Sea Drill. Proj.*, *93*, 1139–1162.

Hinnov, L. A. (2000), New perspectives on orbitally forced stratigraphy, *Annu. Rev. Earth Planet. Sci.*, *28*, 419–475, doi:10.1146/annurev.earth.28.1.419.

Hinnov, L. A., and R. K. Goldhammer (1991), Spectral analysis of the Middle Triassic Latemar Limestone, *J. Sediment. Petrol.*, *61*, 1173–1193.

Huber, B. T., R. D. Norris, and K. G. MacLeod (2002), Deep-sea paleotemperature record of extreme warmth during the Cretaceous, *Geology*, *30*, 123–126, doi:10.1130/0091-7613(2002)030<0123:DSPROE>2.0.CO;2.

Jarvis, I., J. S. Lignum, D. R. Grocke, H. C. Jenkyns, and M. A. Pearce (2011), Black shale deposition, atmospheric CO_2 drawdown, and cooling during the Cenomanian-Turonian Oceanic Anoxic Event, *Paleoceanography*, *26*, PA3201, doi:10.1029/2010PA002081.

Jenkyns, H. C., A. Forster, S. Schouten, and J. S. Sinninghe Damsté (2004), High temperatures in the Late Cretaceous Arctic Ocean, *Nature*, *432*, 888–892, doi:10.1038/nature03143.

Jiménez Berrocoso, A. J., K. G. MacLeod, S. E. Calvert, and J. Elorza (2008), Bottom water anoxia, inoceramid colonization, and benthopelagic coupling during black shale deposition on Demerara Rise (Late Cretaceous western tropical North Atlantic), *Paleoceanography*, *23*, PA3212, doi:10.1029/2007PA001545.

Jiménez Berrocoso, A. J., K. G. MacLeod, E. E. Martin, E. Bourbon, C. I. Londono, and C. Basak (2010), Nutrient trap for Late Cretaceous organic-rich black shales in the tropical North Atlantic, *Geology*, *38*, 1111–1114, doi:10.1130/G31195.1.

Jones, C. E., and H. C. Jenkyns (2001), Seawater strontium isotopes, oceanic anoxic events, and seafloor hydrothermal activity in the Jurassic and Cretaceous, *Am. J. Sci.*, *301*, 112–149, doi:10.2475/ajs.301.2.112.

Kauffman, E. G. (1995), Global change leading to biodiversity crisis in a greenhouse world: The Cenomanian-Turonian (Cretaceous) Mass Extinction, in *Effects of Past Global Change on Life*, edited by S. Stanley et al., pp. 47–71, Natl. Acad. Press, Washington D. C.

Kent, D. V., G. Muttoni, and P. Brack (2004), Magnetostratigraphic confirmation of a much faster tempo for sea-level change for the Middle Triassic Latemar platform carbonates, *Earth Planet. Sci. Lett.*, *228*, 369–377, doi:10.1016/j.epsl.2004.10.017.

Kerr, A. C. (1998), Oceanic plateau formation: A cause of mass extinction and black shale deposition around the Cenomanian-Turonian boundary, *J. Geol. Soc.*, *155*, 619–626, doi:10.1144/gsjgs.155.4.0619.

Kerr, A. C. (2005), Oceanic LIPs: The kiss of death, *Elements*, *1*, 289–292, doi:10.2113/gselements.1.5.289.

Kim, J.-H., S. Schouten, E. C. Hopmans, B. Donner, and J. S. Sinninghe Damsté (2008), Global sediment core-top calibration of the TEX86 palaeothermometer in the ocean, *Geochim. Cosmochim. Acta*, *72*, 1154–1173, doi:10.1016/j.gca.2007.12.010.

Kolonic, S., et al. (2005), Black shale deposition on the northwest African Shelf during the Cenomanian/Turonian oceanic anoxic event: Climate coupling and global organic carbon burial, *Paleoceanography*, *20*, PA1006, doi:10.1029/2003PA000950.

Kuhnt, W., Herbin, J. P., Thurow, J., and J. Wiedmann (1990), Distribution of Cenomanian-Turonian organic facies in the western Mediterranean and along the adjacent Atlantic margin, in *Deposition of Organic Facies*, *AAPG Stud. Geol.*, vol. 30, edited by A. Y. Huc, pp. 133–160, Am. Assoc. of Pet. Geol., Tulsa, Okla.

Kuhnt, W., A. Nederbragt, and L. Leine (1997), Cyclicity of Cenomanian-Turonian organic-carbon-rich sediments in the Tarfaya Atlantic Coastal Basin (Morocco), *Cretaceous Res.*, *18*, 587–601, doi:10.1006/cres.1997.0076.

Kuhnt, W., F. Luderer, S. Nederbragt, J. Thurow, and T. Wagner (2005), Orbital-scale record of the late Cenomanian-Turonian oceanic anoxic event (OAE-2) in the Tarfaya Basin (Morocco), *Int. J. Earth Sci.*, *94*, 147–159, doi:10.1007/s00531-004-0440-5.

Kump, L. R., K. M. Meyer, and A. Ridgwell (2008), Investigating the cause and consequences of oceanic anoxia, *Eos Trans. AGU*, *89*(53), Fall Meeting. Suppl., Abstract PP33D-05.

Kuypers, M. M. M., R. D. Pancost, and J. S. Sinninghe Damsté (1999), A large and abrupt fall in atmospheric CO_2 concentrations during Cretaceous times, *Nature*, *399*, 342–345, doi:10.1038/20659.

Kuypers, M. M. M., L. J. Lourens, W. I. C. Rijpstra, R. D. Pancost, I. A. Nijenhuis, and J. S. Sinninghe Damsté (2004), Orbital forcing of organic carbon burial in the proto-North Atlantic during oceanic anoxic event 2, *Earth Planet. Sci. Lett.*, *228*, 465–482, doi:10.1016/j.epsl.2004.09.037.

Laskar, J., P. Robutel, F. Joutel, M. Gastineau, A. C. M. Correia, and B. Levrard (2004), A long-term numerical solution for the insolation quantities of the Earth, *Astron. Astrophys.*, *428*, 261–285, doi:10.1051/0004-6361:20041335.

Laskar, J., A. Fienga, M. Gastineau, and H. Manche (2011), La:2010: A new orbital solution for the long term motion of the Earth, *Astron. Astrophys.*, *532*, A89, doi:10.1051/0004-6361/201116836.

Liu, Z., M. Pagani, D. Zinniker, R. DeConto, M. Huber, H. Brinkhuis, S. R. Shah, R. M. Leckie, and A. Pearson (2009), Global cooling during the Eocene-Oligocene climate transition, *Science*, *323*, 1187–1190, doi:10.1126/science.1166368.

Locklair, R. E., and B. B. Sageman (2008), Cyclostratigraphy of the Upper Cretaceous Niobrara Formation, Western Interior, U.S.A.: A Coniacian-Santonian orbital timescale, *Earth Planet. Sci. Lett.*, *269*, 540–553, doi:10.1016/j.epsl.2008.03.021.

MacLeod, K. G., E. E. Martin, and S. W. Blair (2008), Nd isotopic excursion across Cretaceous ocean anoxic event 2(Cenomanian-Turonian) in the tropical North, *Atl. Geol.*, *36*, 811–814.

Malinverno, A., E. Erba, and T. Herbert (2010), Orbital tuning as an inverse problem: Chronology of the early Aptian oceanic anoxic event 1a (Selli

Level) in the Cismon APTICORE, *Paleoceanography*, *25*, PA2203, doi:10.1029/2009PA001769.

Martin, E. E., K. G. MacLeod, A. Jiménez Berrocoso, and E. Bourbon (2012), Water mass circulation on Demerara Rise during the Late Cretaceous, *Earth Planet. Sci. Lett.*, *327–328*, 111–120, doi:10.1016/j.epsl.2012.01.037.

März, C., B. Beckmann, C. Franke, C. Vogt, T. Wagner, and S. Kasten (2009), Geochemical environment of the Coniacian-Santonian western tropical Atlantic at Demerara Rise, *Palaeogeogr. Palaeoclimatol. Palaeoecol.*, *273*, 286–301, doi:10.1016/j.palaeo.2008.05.004.

Meyer, K. M., and L. R. Kump (2008), Oceanic Euxinia in Earth History: Causes and consequences, *Annu. Rev. Earth Planet. Sci.*, *36*, 251–288, doi:10.1146/annurev.earth.36.031207.124256.

Meyers, S. R. (2008), Resolving Milankovitchian controversies: The Triassic Latemar Limestone and Eocene Green River Formation, *Geology*, *36*, 319–322, doi:10.1130/G24423A.1.

Meyers, S. R. (2012), Seeing red in cyclic stratigraphy: Spectral noise estimation for astrochronology, *Paleoceanography*, doi:10.1029/2012PA002307, in press.

Meyers, S. R., and B. B. Sageman (2004), Detection, quantification, and significance of hiatuses in pelagic and hemipelagic strata, *Earth Planet. Sci. Lett.*, *224*, 55–72, doi:10.1016/j.epsl.2004.05.003.

Meyers, S. R., and B. B. Sageman (2007), Quantification of deep-time orbital forcing by average spectral misfit, *Am. J. Sci.*, *307*, 773–792, doi:10.2475/05.2007.01.

Meyers, S., B. Sageman, and L. Hinnov (2001), Integrated quantitative stratigraphy of the Cenomanian-Turonian Bridge Creek Limestone Member using evolutive harmonic analysis and stratigraphic modeling, *J. Sediment. Res.*, *71*, 628–644, doi:10.1306/012401710628.

Meyers, S. R., B. B. Sageman, and T. W. Lyons (2005), Organic carbon burial rate and the molybdenum proxy: Theoretical framework and application to Cenomanian-Turonian oceanic anoxic event 2, *Paleoceanography*, *20*, PA2002, doi:10.1029/2004PA001068.

Meyers, S. R., B. B. Sageman, and M. Pagani (2008), Resolving Milankovitch: Consideration of signal and noise, *Am. J. Sci.*, *308*, 770–786, doi:10.2475/06.2008.02.

Meyers, S. R., S. E. Siewert, B. S. Singer, B. B. Sageman, D. J. Condon, J. D. Obradovich, B. R. Jicha, and D. A. Sawyer (2012), Intercalibration of radioisotopic and astrochronologic time scales for the Cenomanian/Turonian Boundary Interval, Western Interior Basin, U.S.A, *Geology*, *40*, 7–10, doi:10.1130/G32261.1.

Mitchell, R. N., D. M. Bice, A. Montanari, L. C. Cleaveland, K. T. Christianson, R. Coccioni, and L. A. Hinnov (2008), Oceanic anoxic cycles? Orbital prelude to the Bonarelli Level (OAE 2), *Earth Planet. Sci. Lett.*, *267*, 1–16, doi:10.1016/j.epsl.2007.11.026.

Moriya, K., P. Wilson, O. Friedrich, J. Erbacher, and H. Kawahata (2007), Testing for ice sheets during the mid-Cretaceous greenhouse using glassy foraminiferal calcite from the mid-Cenomanian tropics on Demerara Rise, *Geology*, *35*, 615–618, doi:10.1130/G23589A.1.

Mudelsee, M. (2010), *Climate Times Series Analysis: Classical Statistical and Bootstrap Methods*, 474 pp., Springer, Dordrecht, Netherlands.

Muller, R. A., and G. J. MacDonald (2000), *Ice Ages and Astronomical Causes*, 318 pp., Springer, Chichester, U. K.

Nederbragt, A. J., J. Thurow, and R. Pearce (2007), Sediment composition and cyclicity in the Mid-Cretaceous at Demerara Rise, ODP Leg 207, *Proc. Ocean Drill. Program, Sci. Results*, *207*, doi:10.2973/odp.proc.sr.207.103.2007.

Norris, R. D., D. Kroon, B. T. Huber, and J. Erbacher (2001), Cretaceous-Paleogene ocean and climate change in the subtropical North Atlantic, in *Western North Atlantic Palaeogene and Cretaceous Palaeoceanography*, edited by D. Kroon, R. D. Norris, and A. Klaus, *Geol. Soc. Spec. Publ.*, *183*, 1–22, doi:10.1144/GSL.SP.2001.183.01.01.

Park, J., and T. Herbert (1987), Hunting for paleoclimatic periodicities in a geologic time series with an uncertain time scale, *J. Geophys. Res.*, *92*, 14,027–14,040, doi:10.1029/JB092iB13p14027.

Preto, N., L. A. Hinnov, L. A. Hardie, and V. De Zanche (2001), Middle Triassic orbital signature recorded in the shallow-marine Latemar carbonate buildup (Dolomites, Italy), *Geology*, *29*, 1123–1126, doi:10.1130/0091-7613(2001)029<1123:MTOSRI>2.0.CO;2.

Prokoph, A., M. Villeneuve, F. P. Agterberg, and V. Rachold (2001), Geochronology and calibration of global Milankovitch cyclicity at the Cenomanian-Turonian boundary, *Geology*, *29*, 523–526, doi:10.1130/0091-7613(2001)029<0523:GACOGM>2.0.CO;2.

Sageman, B. B., J. Rich, M. A. Arthur, G. E. Birchfield, and W. E. Dean (1997), Evidence For Milankovitch periodicities in Cenomanian-Turonian lithologic and geochemical cycles, Western Interior U.S.A., *J. Sediment. Res.*, *67*, 286–301.

Sageman, B., J. Rich, C. E. Savrda, T. Bralower, M. A. Arthur, and W. E. Dean (1998), Multiple Milankovitch cycles in the Bridge Creek Limestone (Cenomanian-Turonian), Western Interior basin, in *Stratigraphy and Paleoenvironments of the Cretaceous Western Interior Seaway, U.S.A.*, *Concepts Sedimentol. Paleontol.*, vol. 6, edited by W. E. Dean and M. A. Arthur, pp. 153–171, Soc. for Sediment. Geol., Tulsa, Okla.

Sageman, B. B., S. R. Meyers, and M. A. Arthur (2006), Orbital time scale and new C-isotope record for Cenomanian-Turonian boundary stratotype, *Geology*, *34*, 125–128, doi:10.1130/G22074.1.

Shah, S. R., G. Mollenhauer, N. Ohkouchi, T. I. Eglinton, and A. Pearson (2008), Origins of archaeal tetraether lipids in sediments: Insights from radiocarbon analysis, *Geochim. Cosmochim. Acta*, *72*, 4577–4594, doi:10.1016/j.gca.2008.06.021.

Shen, Y. N., D. E. Canfield, and A. H. Knoll (2002), Middle Proterozoic ocean chemistry: Evidence from the McArthur Basin, northern Australia, *Am. J. Sci.*, *302*, 81–109, doi:10.2475/ajs.302.2.81.

Shipboard Scientific Party (2004), Leg 207 summary, *Proc. Ocean Drill. Program, Initial Rep.*, *207*, 293–317.

Sinninghe Damsté, J. S., M. M. Kuypers, R. D. Pancost, and S. Schouten (2008), The carbon isotopic response of algae, (cyano)bacteria, archaea and higher plants to the late Cenomanian perturbation of the global carbon cycle: Insights from biomarkers in black shales from the Cape Verde Basin (DSDP Site 367), *Org. Geochem.*, *39*, 1703–1718, doi:10.1016/j.orggeochem.2008.01.012.

Sinninghe Damsté, J. S., E. C. van Bentum, G.-J. Reichart, J. Pross, and S. Schouten (2010), A CO_2 decrease-driven cooling and increased latitudinal temperature gradient during the mid-Cretaceous Oceanic Anoxic Event 2, *Earth Planet. Sci. Lett.*, *293*, 97–103, doi:10.1016/j.epsl.2010.02.027.

Sinton, C. W., and R. A. Duncan (1997), Potential links between ocean plateau volcanism and global ocean anoxia at the Cenomanian-Turonian boundary, *Econ. Geol.*, *92*, 836–842, doi:10.2113/gsecongeo.92.7-8.836.

Snow, L. J., R. A. Duncan, and T. J. Bralower (2005), Trace element abundances in the Rock Canyon Anticline, Pueblo, Colorado, marine sedimentary section and their relationship to Caribbean plateau construction and oxygen anoxic event 2, *Paleoceanography*, *20*, PA3005, doi:10.1029/2004PA001093.

Thomson, D. J. (1982), Spectrum estimation and harmonic analysis, *Proc. IEEE*, *70*, 1055–1096, doi:10.1109/PROC.1982.12433.

Thomson, D. J. (1990), Quadratic-inverse spectrum estimates: Applications to palaeoclimatology, *Philos. Trans. R. Soc. London, Ser. B*, *332*, 539–597, doi:10.1098/rsta.1990.0130.

Thomson, D. J. (2010), Time-series analysis of paleoclimate data, in *Encyclopedia of Paleoclimatology and Ancient Environments*, edited by V. Gornitz, pp. 949–959, Springer, New York.

Trabucho Alexandre, J. T., E. Tuenter, G. A. Henstra, K. J. van der Zwan, R. S. W. van de Wal, H. A. Dijkstra, and P. L. de Boer (2010), The mid-Cretaceous North Atlantic nutrient trap: Black shales and OAEs, *Paleoceanography*, *25*, PA4201, doi:10.1029/2010PA001925.

Tsikos, H., et al. (2004), Carbon-isotope stratigraphy recorded by the Cenomanian-Turonian Oceanic Anoxic Event: Correlation and implications based on three localities, *J. Geol. Soc.*, *161*, 711–719, doi:10.1144/0016-764903-077.

Turgeon, S. C., and R. A. Creaser (2008), Cretaceous oceanic anoxic event 2 triggered by a massive magmatic episode, *Nature*, *454*, 323–326, doi:10.1038/nature07076.

van Bentum, E. C., G.-J. Reichart, A. Forster, and J. S. Sinninghe Damsté (2012), Latitudinal differences in the amplitude of the OAE-2 carbon isotopic excursion: pCO_2 and paleo productivity, *Biogeosciences*, *9*, 717–731, doi:10.5194/bg-9-717-2012.

Vaughan, S., R. J. Bailey, and D. G. Smith (2011), Detecting cycles in stratigraphic data: Spectral analysis in the presence of red noise, *Paleoceanography*, *26*, PA4211, doi:10.1029/2011PA002195.

Voigt, S., A. S. Gale, and S. Flogel (2004), Midlatitude shelf seas in the Cenomanian-Turonian greenhouse world: Temperature evolution and North Atlantic circulation, *Paleoceanography*, *19*, PA4020, doi:10.1029/2004PA001015.

Voigt, S., A. S. Gale, and T. Voigt (2006), Sea-level change, carbon cycling and palaeoclimate during the Late Cenomanian of northwest Europe; an integrated palaeoenvironmental analysis, *Cretaceous Res.*, *27*, 836–858, doi:10.1016/j.cretres.2006.04.005.

Voigt, S., J. Erbacher, J. Mutterlose, W. Weiss, T. Westerhold, F. Wiese, M. Wilmsen, and T. Wonik (2008), The Cenomanian-Turonian of the Wunstorf section- (North Germany): Global stratigraphic reference section and new orbital time scale for Oceanic Anoxic Event 2, *Newsl. Stratigr.*, *43*, 65–89, doi:10.1127/0078-0421/2008/0043-0065.

Weedon, G. P. (2003), *Time-Series Analysis and Cyclostratigraphy*, Cambridge Univ. Press, Cambridge, U. K., doi:10.1017/CBO9780511535482.

Weedon, G. P., and H. C. Jenkyns (1999), Cyclostratigraphy and the Early Jurassic timescale: Data from the Belemnite Marls, Dorset, southern England, *Geol. Soc. Am. Bull.*, *111*, 1823–1840, doi:10.1130/0016-7606(1999)111<1823:CATEJT>2.3.CO;2.

Westerhold, T., and U. Röhl (2009), High resolution cyclostratigraphy of the early Eocene - New insights into the origin of the Cenozoic cooling trend, *Clim. Past*, *5*, 309–327, doi:10.5194/cp-5-309-2009.

Whittaker, S. G., and T. K. Kyser (1993), Variations in the neodymium and strontium isotopic composition and REE content of molluscan shells from the Cretaceous Western Interior seaway, *Geochim. Cosmochim. Acta*, *57*, 4003–4014, doi:10.1016/0016-7037(93)90349-2.

Zühlke, R., T. Bechstadt, and R. Mundil (2003), Sub-Milankovitch and Milankovitch forcing on a model Mesozoic carbonate platform—The Latemar (Middle Triassic, Italy), *Terra Nova*, *15*, 69–80, doi:10.1046/j.1365-3121.2003.00366.x.